

## Research



**Cite this article:** Michaels TCT, Kusters R, Dear AJ, Storm C, Weaver JC, Mahadevan L. 2019 Geometric localization in supported elastic struts. *Proc. R. Soc. A* **475**: 20190370. <http://dx.doi.org/10.1098/rspa.2019.0370>

Received: 12 June 2019

Accepted: 7 August 2019

**Subject Areas:**

materials science, applied mathematics, mechanics

**Keywords:**

localization, elasticity, pattern formation

**Author for correspondence:**

L. Mahadevan

e-mail: [lmahadev@g.harvard.edu](mailto:lmahadev@g.harvard.edu)

<sup>†</sup>These authors contributed equally to this study.

Electronic supplementary material is available online at <https://doi.org/10.6084/m9.figshare.c.4643474>.

# Geometric localization in supported elastic struts

T. C. T. Michaels<sup>1,†</sup>, R. Kusters<sup>2,3,†</sup>, A. J. Dear<sup>1</sup>,  
C. Storm<sup>2,4</sup>, J. C. Weaver<sup>5</sup> and L. Mahadevan<sup>1,6,7,8</sup>

<sup>1</sup>Paulson School of Engineering and Applied Sciences, Harvard University, Cambridge, MA, USA

<sup>2</sup>Department of Applied Physics, Eindhoven University of Technology, Eindhoven, The Netherlands

<sup>3</sup>University Paris Descartes, Center for Research and Interdisciplinarity (CRI), 10 Rue Charles V, Paris, France

<sup>4</sup>Institute for Complex Molecular Systems, Eindhoven University of Technology, Eindhoven, The Netherlands

<sup>5</sup>Wyss Institute for Biologically Inspired Engineering, Harvard University, Boston, MA, USA

<sup>6</sup>Department of Organismic and Evolutionary Biology, <sup>7</sup>Department of Physics, and <sup>8</sup>Kavli Institute for Nanobio Science and Technology, Harvard University, Cambridge, MA, USA

RK, 0000-0002-9561-2303; LM, 0000-0002-5114-0519

Localized deformation patterns are a common motif in morphogenesis and are increasingly finding applications in materials science and engineering, in such instances as mechanical memories. Here, we describe the emergence of spatially localized deformations in a minimal mechanical system by exploring the impact of growth and shear on the conformation of a semi-flexible filament connected to a pliable shearable substrate. We combine numerical simulations of a discrete rod model with theoretical analysis of the differential equations recovered in the continuum limit to quantify (in the form of scaling laws) how geometry, mechanics and growth act together to give rise to such localized structures in this system. We find that spatially localized deformations along the filament emerge for intermediate shear modulus and increasing growth. Finally, we use experiments on a 3D-printed multi-material model system to demonstrate that external control of the amount of shear and growth may be used to regulate the spatial extent of the localized strain texture.

# 1. Introduction

The deformation of spatially extended elastic structures, such as filaments, plates and shells is often elastically constrained by the surrounding medium. The simplest formulation of this elastic constraint is due to Winkler [1] who proposed a local linear elastic model for the medium. Since then, there have been many variants of the Winkler model that account for both non-locality and nonlinearity, particularly in the context of localized deformations in such systems that take the form of creases, localized wrinkles, etc. [2–12]. These localized patterns in spatially extended dynamical systems are not limited to elasticity; indeed they are of intrinsic interest due to their potential role as mediators of turbulence in fluids, optics and beyond [13–16]. In the context of elasticity, a recent proposal suggests the use of localized dimples as programmable elastic bits (e-bits) to store memory on a featureless elastic shell that requires minimal substrate infrastructure [17], and raises the question of whether there are alternatives that take advantage of substrate elasticity to confine deformations and thus generalize these ideas to a much broader class of systems.

In this paper, we address this question by studying the appearance of localized structures in a minimal model system of an extensible growing adherent filament that is attached to a rigid substrate by a set of stretchable and shearable springs. Using a combination of theory, simulations and experiments, we show that this minimal system can give rise to robust spatial localization as a function of growth and shear. More specifically, we derive explicit scaling relationships describing the extent and amplitude of localized deformations, as well as a phase diagram describing the range of mechanical parameters that admit localized structures. We then demonstrate these rules in practice using a 3D-printed multi-material model system. Our results identify the physical parameters that control the extent of localization, suggesting a strategy for easy and robust programming of mechanical deformations at multiple scales.

# 2. Theory

Our physical model of geometric localization is a flexible filament that can swell or grow in length, but is constrained by an elastic substrate to which it is attached. The filament can bend transversely and stretch longitudinally, while the substrate resists lateral shear and transverse stretch induced by the filament. We consider two limits of this problem: (i) a *discrete* version, where the filament is assumed to be made of a set of rigid links with soft connectors that resist bending, connected to a substrate via a set of discrete springs that resist changes in their natural length and orientation relative to the rigid rods (figure 1), and (ii) a *continuum* version, which maps onto the growth of a filament embedded in an elastic medium. In either case, we seek the solution with minimal total elastic energy for a filament with initial rest length  $L$  which has grown/swollen to a total length of  $L(1 + \epsilon)$ , where  $\epsilon$  measures the relative growth (i.e. strain) of the filament.

## (a) Discrete rod model

The discrete rod model consists of a flexible filament made of  $n_s$  discrete segments of rest length  $\ell_0$  attached to a solid substrate through a set of  $N$  Hookean springs that can extend vertically and shear horizontally (figure 1). The total energy of the discrete rod model is

$$\mathcal{E} = \frac{\bar{S}}{2\ell_0} \sum_{n=1}^{n_s} (\ell_n - \ell_0)^2 + \frac{\bar{B}}{\ell_0} \sum_{n=1}^{n_s-1} (1 - \cos \theta_{n,n+1}) + \frac{\bar{K}}{2b} \sum_{i=1}^N (h_i - h_0)^2 + \frac{\bar{G}}{2} \sum_{i=1}^N \alpha_i^2, \quad (2.1)$$

where  $\bar{S}$  denotes the filament stretching stiffness,  $\bar{B}$  is the bending rigidity of the filament,  $\bar{K}$  is the spring stiffness and  $\bar{G}$  is the shear modulus of the springs. Moreover,  $\ell_n$  is the length of the  $n$ -th filament segment,  $b = L/N$  is the spacing between the adherent springs, where  $L = n_s \ell_0$  is the total length of the supporting filament. In equation (2.1), the first two terms correspond to the stretching and bending energies of the filament, while the last two terms correspond to the

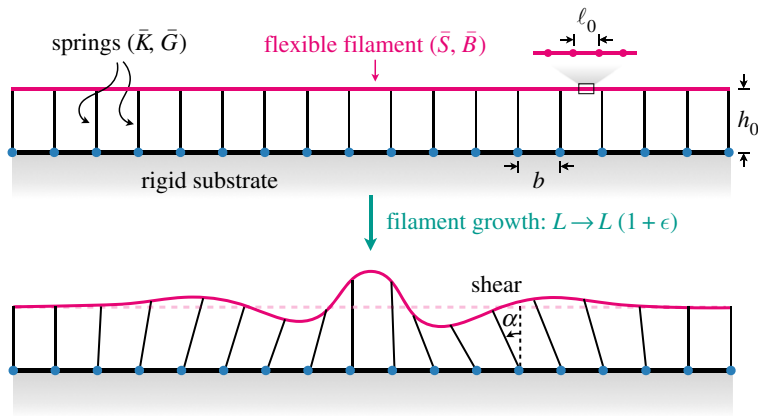


**Figure 1.** Schematic of the discrete rod model of geometric localization. A flexible filament (with stretching stiffness  $\bar{S}$  and bending stiffness  $\bar{B}$ ) is attached to a rigid substrate through an array of springs that can extend vertically (with spring stiffness  $\bar{K}$ ) and shear horizontally (with shear modulus  $\bar{G}$ ). The flexible filament undergoes uniform growth, such that its rest length  $L$  increases to  $L(1 + \epsilon)$ , where  $\epsilon$  is the growth strain. Depending on shear modulus  $\bar{G}$ , filament growth  $\epsilon$  can result in the formation of localized deformation patterns. Understanding the conditions for the emergence of such localized deformations as a function of mechanical parameters is the subject of this paper. (Online version in colour.)

stretching and shear energies of the springs connecting the filament to the rigid substrate. The bending energy is consistent with the semi-flexible approximation valid for weak bending, where  $\cos \theta_{i,i+1} = \hat{t}_i \cdot \hat{t}_{i+1}$ ,  $i = 1, \dots, n_s$ , with  $\hat{t}_i$  being the unit tangent vector of the  $i$ -th filament segment,  $\alpha_i$  denoting the angle that the  $i$ -th spring makes with the vertical, hence measuring the amount of shear;  $h_i$  being the vertical extension of the  $i$ -th spring and  $h_0$  is the rest length of the springs.

The procedure we use to ‘grow’ the filament is as follows: we start with a configuration where the springs are in their rest configuration and vertical, and the filament is straight and horizontal. We then increase the rest length of the filament segments  $\ell_0$  by a small amount  $\epsilon \ell_0$ , i.e.  $\ell_0 \rightarrow \ell_0(1 + \epsilon)$ . Since thin rods are much easier to bend than to stretch, we focus our analysis on filaments with  $\bar{S} \gg \bar{K}$ ; some extensibility is retained for increased numerical stability. To minimize the total energy  $\mathcal{E}$  of the system, we either use Newton’s method, present in the FindMinimum routine, or a global energy search present in the NMinimize routine, implemented in MATHEMATICA (see electronic supplementary material, S2).

## (b) Continuous model

To determine how localized filament deformations emerge during growth, we map the discrete rod model onto a set of coupled differential equations that describe the growth of the adhering filament in the continuum limit, valid for small deformations. To this end, we consider the elastic energy equation (2.1) in the limits  $b, \ell_0 \rightarrow 0$  and  $N, n_s \rightarrow \infty$  with  $Nb = n_s \ell_0 = L$  being constant. In this limit, the total elastic energy  $\mathcal{E}$  of the system with continuous horizontal  $U(x)$  and vertical  $W(x)$  displacements as functions of the arclength  $x$  is given by (see electronic supplementary material, S1):

$$\mathcal{E} = \int_{L(1+\epsilon)} \left( \frac{S}{2} \left[ U'(x) + \frac{W'(x)^2}{2} - \epsilon \right]^2 + \frac{B}{2} W''(x)^2 + \frac{K}{2} W(x)^2 + \frac{G}{2} U(x)^2 \right) dx. \quad (2.2)$$

The elastic constants in the continuum model relate to those in the discrete model (denoted with bar) through  $G = \bar{G}/(h_0^2 b)$ ,  $K = \bar{K}/b^2$ ,  $S = \bar{S}b/\ell_0$  and  $B = \bar{B}/h_0$  (see electronic supplementary material, S1). The various energy terms in equation (2.2) have a straightforward physical

interpretation: the first term is the stretching energy of the filament and is proportional to the square of the elastic strain  $\epsilon_{\text{el}} = \epsilon_{\text{tot}} - \epsilon$ , where  $\epsilon_{\text{tot}}$  is the total strain and  $\epsilon$  is the growth strain. The second term in equation (2.2), proportional to the square of the local curvature  $W''(x)$ , describes the bending energy of the filament. The last two terms in equation (2.2) correspond to the energy contributions associated with the stretching and the shear of the substrate; these contributions are proportional to the squares of the vertical and horizontal displacement fields, respectively.

To find the system configurations of minimal total energy, we consider the Euler–Lagrange equations associated with equation (2.2),  $\delta\mathcal{E}/\delta W(x) = \delta\mathcal{E}/\delta U(x) = 0$ , which read (see electronic supplementary material, S1.6):

$$BW''''(x) + S \left[ \epsilon - U'(x) - \frac{W'(x)^2}{2} \right] W''(x) + KW(x) - GU(x)W'(x) = 0 \quad (2.3a)$$

and

$$S [U''(x) + W'(x)W''(x)] - GU(x) = 0. \quad (2.3b)$$

We used a shooting algorithm to numerically solve the nonlinear system equation (2.3) subject to clamped boundary conditions  $U(-L/2) = U(L/2) = 0$ ,  $W(-L/2) = W(L/2) = 0$ ,  $W'(-L/2) = W'(L/2) = 0$  (see electronic supplementary material, S2). Note that these equations decouple and are fully integrable in two limits: (i) for  $G \rightarrow \infty$ , and (ii) for  $G = 0$ . Both situations lead to a uniform wrinkling solution with characteristic wavelength  $\lambda = (B/K)^{1/4}$  (see electronic supplementary material, S3.2 and S3.3).

### 3. Analysis

Before turning to an approximate analytical approach to the nonlinear system equation (2.3), we describe the results of numerical simulations of the discrete and continuous problems that shed light on the conditions for the existence of spatially localized solutions.

#### (a) Lowering shear modulus induces localization

Simulating the discrete rod model under different conditions of growth  $\epsilon$  and shear modulus  $\bar{G}$  for clamped and free filament edges, we see that for the case of clamped edges, increasing  $\epsilon$  above a critical threshold  $\epsilon^*$  and for large shear modulus  $\bar{G}$ , results in a uniform periodically buckled state (figure 2a). This situation is consistent with the solution with the classical Winkler foundation [1], corresponding to the case when  $\bar{G} \rightarrow \infty$ , i.e. the springs can extend only vertically. If we decrease  $\bar{G}$ , allowing for the adherent springs to rotate, we find that, upon uniform growth  $\epsilon$ , the vertical displacement field along the filament is not uniformly periodic, but rather becomes localized (figure 2b). Since the filament itself is effectively inextensible ( $\bar{S}/\bar{K} = 10^3$ ), this localized strain solution is accompanied by a shear field of the adherent springs, accompanied by a non-uniform horizontal displacement of the substrate. While the buckling wavelength remains unaltered, we find that localization is favoured by increasing  $\epsilon$  (figure 2c) or decreasing  $\bar{G}$  (figure 2d). Decreasing the shear modulus further leads to an increase of the localization width. Eventually, for vanishing shear modulus  $\bar{G} = 0$ , we again recover the uniform periodically buckled solution that exists over the entire length of the filament.

Changing the boundary conditions changes the results; e.g. releasing the edges results in the occurrence of localized structures that occur near the filament edge and upon further growth travel inward. In electronic supplementary material, S2, we discuss this aspect further.

#### (b) Localized deformations as solutions to the continuous equations

To rationalize the emergence of spatial localized deformations in terms of specific combinations of the underlying physical parameters, we set out to solve the continuous equations, equation (2.3),

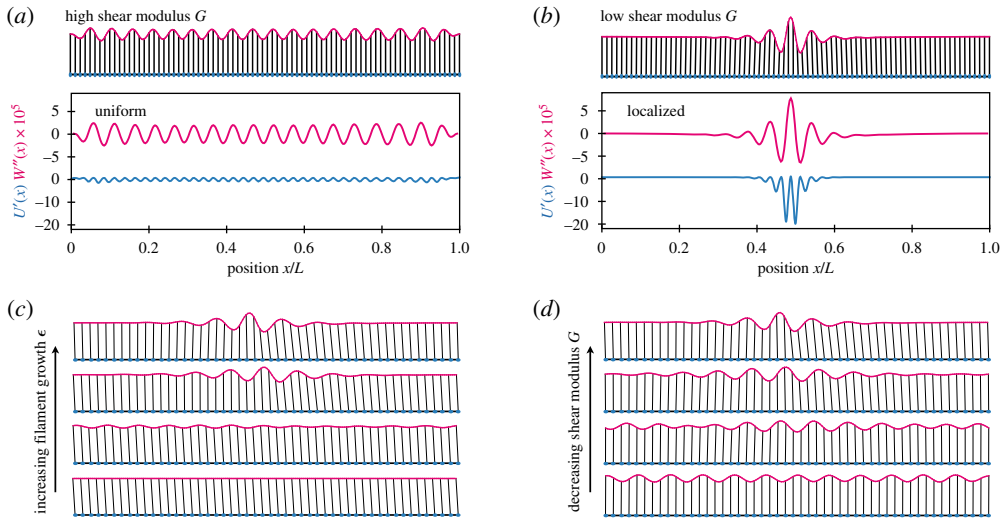


**Figure 2.** Computer simulations of discrete rod model. (a–b) Depending on the shear modulus of the springs, filament growth results in uniform buckling for high shear modulus  $\bar{G} = 0.01$  (a), and localized deformations for low shear modulus  $\bar{G} = 0.0002$  (b). In both cases  $N = 100$ ,  $n_s = 316$ ,  $b = 1$ ,  $h_0 = 1$ ,  $\bar{K} = 0.1$ ,  $\bar{S} = 100$ ,  $\bar{B} = 0.4$  and  $\epsilon = 3.8\%$ . (a,b) The curvature ( $W'' \times 10^5$ , top purple line) and strain ( $U'$ , bottom blue line) fields along the filament. (c–d) Filament deformations for increasing growth strain  $\epsilon$  (c), and decreasing shear modulus for the springs  $\bar{G}$  (d). In (c), growth strain is  $\epsilon = 0.0004, 0.012, 0.059$  and  $0.075$  (bottom to top) at constant shear rate  $\bar{G} = 0.002$ . In (d), the shear modulus is  $\bar{G} = 0.05, 0.01, 0.005$  and  $0.002$  (bottom to top) for  $\epsilon = 0.075$ . In both (c,d),  $N = 50$ . (Online version in colour.)

analytically in the limit of low shear modulus  $G$  by employing weakly nonlinear analysis [18]. We construct this solution on the half-axis  $0 \leq x \leq L/2$  by employing the mirror-symmetry of the vertical displacement around the midpoint  $x = 0$  (see electronic supplementary material, S3).

### (i) Linear theory and bifurcation analysis

As a first step, we study the linearized equations  $BW''''(x) + S\epsilon W''(x) + KW(x) = 0$ ,  $SU'''(x) = GU(x)$  subject to the boundary conditions associated with clamped edges (see electronic supplementary material, S3.1). For  $\epsilon \leq \epsilon^*$ , where

$$\epsilon^* = \frac{2\sqrt{BK}}{S}, \quad (3.1)$$

we find that the only solution consistent with the boundary conditions is  $W(x) = U(x) = 0$ , i.e. no deformation. However, for  $\epsilon \geq \epsilon^*$ , we find a non-trivial, uniformly periodic wrinkling solution for the vertical displacement; the wavelength of wrinkling is  $\lambda = (B/K)^{1/4}$ , consistent with the classical literature [19,20]. Thus, analysis of the linearized equations implies a bifurcation point when  $\epsilon = \epsilon^*$  (figure 3b). The physical interpretation of  $\epsilon^*$  is the maximal amount of strain that can be accommodated by filament stretching (compression) without causing any bending and spring deformation. Indeed,  $\epsilon^*$  is inversely proportional to  $S$ ; decreasing  $S$  leads to a higher strain threshold  $\epsilon^*$ . Above the critical swelling/growth strain  $\epsilon^*$ , the excess strain  $\epsilon - \epsilon^*$  is accommodated by filament buckling.

### (ii) Weakly nonlinear theory

The linear theory implies that localized deformations exist for equation (2.3) only for  $\epsilon > \epsilon^*$ ; we thus consider the nonlinear terms in equation (2.3) as a perturbation of the linearized equations in excess strain  $\epsilon - \epsilon^*$ . To do so, we rescale variables as  $\tilde{x} = x/\lambda$ ,  $W = \sqrt{\epsilon - \epsilon^*} \lambda \tilde{W}$  and  $U(x) = (\epsilon - \epsilon^*) \lambda \tilde{U}$ , solve the resulting equation for  $U(x)$  exploiting  $(G/S)\sqrt{B/K} \ll 1$  and insert this

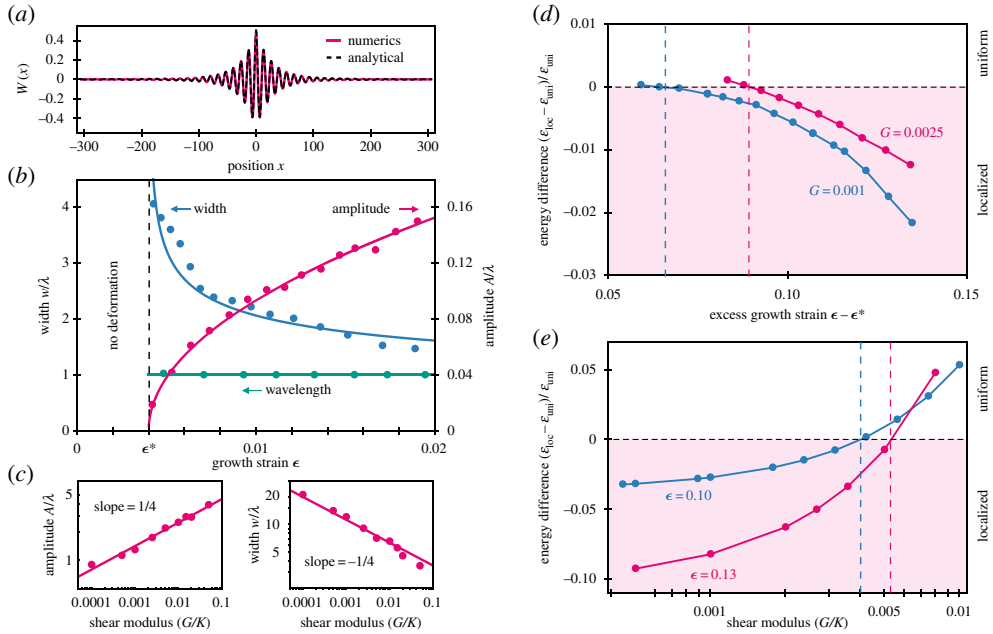


**Figure 3.** Theoretical analysis of geometric localization. (a) Vertical displacement field  $W(x)$  obtained by numerical integration of equation (2.3) (solid line) and comparison to the analytical perturbation solution, equation (3.5) (black dotted line). Parameters:  $G = 5 \times 10^{-5}$ ,  $S = 10$ ,  $B = 0.2$ ,  $K = 0.01$ ,  $\epsilon = 9.5 \times 10^{-3}$ ,  $L = 23 \times \lambda$ . (b) Bifurcation diagram for equation (2.3) as a function of growth strain  $\epsilon$ . For  $\epsilon < \epsilon^*$ , there is no deformation, while for  $\epsilon > \epsilon^*$  either uniform or localized deformations emerge. For  $\epsilon > \epsilon^*$ , the amplitude of deformations increases in proportion to  $\sqrt{\epsilon - \epsilon^*}$ , as predicted by equation (3.5) (solid line). The figure also shows the width  $w$  and wavelength  $\lambda$  of localized deformations as a function of  $\epsilon$ , with solid lines indicating the theoretical predictions. Data points are from numerical simulations of the discrete rod model for the following parameters:  $N = 80$ ,  $\bar{S} = 100$ ,  $b = 1$ ,  $n_s = 316$ ,  $\bar{K} = 0.1$ ,  $\bar{B} = 0.4$  and  $\bar{G} = 0.001$ . (c) Double logarithmic plots of amplitude  $A$  and width  $w$  of localized solutions as function of shear modulus  $G$ . The solid lines, which have slopes of  $1/4$ , respectively,  $-1/4$ , are the theoretical predictions of equations (3.7) and (3.6),  $A \propto G^{1/4}$ ,  $w \propto G^{-1/4}$ . Simulation parameters:  $S = 10$ ,  $B = 1$ ,  $K = 1$ ,  $\epsilon = 0.21$ ,  $L = 20 \times \lambda$ . (d–e) Above the bifurcation point  $\epsilon^*$ , uniform or localized deformations are selected depending on their relative energies, as described by  $(\mathcal{E}_{loc} - \mathcal{E}_{uni})/\mathcal{E}_{uni}$ , where  $\mathcal{E}_{loc}$  is the energy of the localized state and  $\mathcal{E}_{uni}$  is the energy of the uniform state. (d) Shows that, at constant  $G$ , there is a critical value for  $\epsilon$  above which the localized solution has lower energy compared to the uniform buckled solution. The critical  $\epsilon$  increases with increasing  $G$ . (e) Shows that, at constant  $\epsilon$ , there is a critical shear modulus  $G$ , below which the localized solution is lower in energy than the uniform deformation. The critical  $G$  increases with increasing  $\epsilon$ . Simulation parameters for (d–e) are:  $N = 50$ ,  $\bar{S} = 100$ ,  $b = 1$ ,  $n_s = 197$ ,  $\bar{K} = 0.1$ ,  $\bar{B} = 0.4$ ,  $\bar{G} = 0.001, 0.0025$  and  $\epsilon = 0.1, 0.13$  as indicated on the graph. (Online version in colour.)

solution back into equation (2.3). This procedure (detailed in electronic supplementary material, S3.5) yields at leading order:

$$\bar{W}''''(\bar{x}) + 2\bar{W}''(\bar{x}) + \bar{W}(\bar{x}) - \delta \frac{(\bar{x} - \bar{L}/2)^2}{2} \bar{W}''(\bar{x}) = 0, \quad (3.2)$$

where the relevant perturbation parameter of the problem emerges as  $\delta = (G/K)(\epsilon - \epsilon^*) \ll 1$ . In equation (3.2), we recognize the linear part, which yields uniform buckling with wavelength  $\lambda$ ; as expected, we obtain a new term, proportional to  $\delta$ , which comes from the excess strain  $\epsilon - \epsilon^*$  and varies slowly on distances of scale  $\lambda$ . This problem is analogous to the WKB approximation to the Schrödinger equation with a slowly varying potential. The form of equation (3.2) thus suggests the following envelope-type ansatz for the vertical displacement

$$\bar{W}(x) = A(\delta^{1/4} \bar{x}) e^{i\bar{x}} + \text{c.c.} \quad (3.3)$$



where  $A$  is a slow-varying amplitude (envelope) function that depends on the slow variable  $X = \delta^{1/4}\bar{x}$  and c.c. stands for complex conjugate. Inserting this ansatz into equation (3.2) and collecting terms at various orders in  $\delta^{1/4}$ , we arrive at the following amplitude equation describing the long-scale behaviour of the solution (see electronic supplementary material, S3.6):

$$\frac{\partial^2 A(X)}{\partial X^2} = \frac{(X - X_e)^2}{8} A(X), \quad (3.4)$$

where  $X_e = \delta^{1/4}L/\lambda$ . The amplitude equation is a particular case of the Weber differential equation  $y''(z) + (\nu + 1/2 - z^2/4)y(z) = 0$  with  $\nu = -1/2$ , whose solution is expressed in terms of the parabolic cylinder function  $y(z) = D_{-1/2}(z)$  [21]. Hence, the final perturbation solution for the vertical displacement is given by:

$$W(x) \propto \sqrt{\epsilon - \epsilon^*} \lambda \cos\left(\frac{x}{\lambda}\right) D_{-1/2}\left[\left(\epsilon - \epsilon^*\right)^{1/4} \left(\frac{G}{2B}\right)^{1/4} \left(x - \frac{L}{2}\right)\right]. \quad (3.5)$$

The solution has the form of the uniform wrinkled solution  $\cos(x/\lambda)$  modulated by an envelope function  $A(X)$ , which depends on the slow variable  $X = (\epsilon - \epsilon^*)^{1/4}(G/B)^{1/4}x$ . Note that, independently of growth strain  $\epsilon$  or shear modulus  $G$ , the solution always selects the wavelength  $\lambda$ . The accuracy of equation (3.5) against numerical integration of equation (2.3) is shown in figure 3*a* and in electronic supplementary material, figures S7–S10.

### (iii) Scaling laws for localized solution

With a perturbative solution to the continuous equations equation (2.3) at hand, we can now predict the scaling behaviour of a number of key observables, such as the width  $w$ , the wavelength  $\lambda$  and the amplitude  $A$  of the localized deformations. In particular, from equation (3.5), the width  $w$  of the localization scales as:

$$\frac{w}{\lambda} \propto \delta^{-1/4} = (\epsilon - \epsilon^*)^{-1/4} \left(\frac{G}{K}\right)^{-1/4}. \quad (3.6)$$

Hence, increasing growth strain  $\epsilon$  beyond the bifurcation point  $\epsilon^*$ , or increasing  $G$  favours localization (figure 3*b,c*). The wavelength of the localized deformation  $\lambda = (B/K)^{1/4}$  is independent of growth strain  $\epsilon$  and shear modulus  $G$  (figure 3*b*). Finally, the amplitude  $A$  of the localization scales as

$$\frac{A}{\lambda} \propto (\epsilon - \epsilon^*)^{1/2} \left(\frac{G}{K}\right)^{1/4} \left(\frac{L}{\lambda}\right)^{1/2}. \quad (3.7)$$

We have tested these scaling predictions using numerical realizations of the continuous equations (2.3) obtained with a shooting algorithm. As shown in figure 3*b,c* and electronic supplementary material, figure S11, the scaling relationships of equations (3.6) and (3.7) with  $\epsilon$  and  $G$  are verified by numerical analysis, thus confirming that we can capture the key aspects of the localized solutions.

### (c) Energetics of localized solution

Turning from the form of the solutions to their stability requires us to study the relative energetics of the localized and uniform buckled solutions (see also electronic supplementary material, S2 for details on the energy calculation procedure). In figure 3*d*, we plot the energy difference between localized and uniform buckling deformations,  $(\mathcal{E}_{\text{loc}} - \mathcal{E}_{\text{uni}})/\mathcal{E}_{\text{uni}}$ , as a function of the excess strain  $\epsilon - \epsilon^*$  at fixed values of shear modulus  $G$ . We find that there is a critical strain  $\epsilon$  above which the localized solution has lower energy than the uniform solution; this critical strain increases with increasing  $G$  or decreasing  $K$ . In fact, the energy difference between the localized and the uniform states is set by the interplay between shear energy and extensional energy of the substrate springs; localizing the strain of the filament increases the amount of shear, while decreasing the extensional energy of the substrate springs (see electronic supplementary material, S3.7).

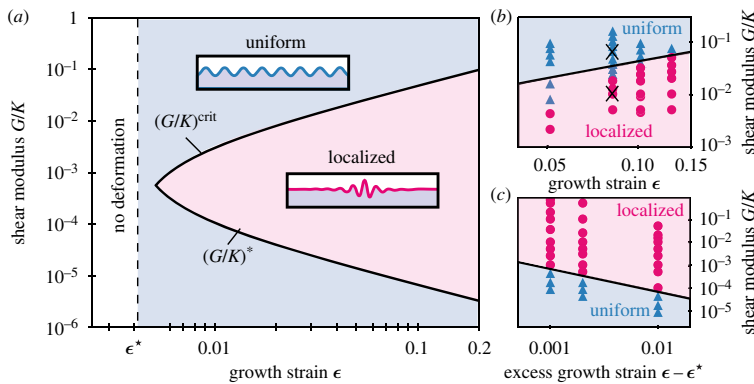


**Figure 4.** Phase diagram as a function of shear modulus  $G/K$  and growth strain  $\epsilon$  separating regions where uniform or localized buckling deformations are minimum energy solutions. (a) In the purple region, bounded by the theoretical lines  $(G/K)^{crit}$  and  $(G/K)^*$ , localized deformations exist and have lower energy than uniform solutions. Diagram calculated for the same parameters as in figure 3d. (b) Phase diagram in high  $G$  regime obtained from numerical simulations of discrete rod model for the parameters of figure 3d and comparison with theoretical prediction (solid line). Circles indicate localized deformations, triangles indicate uniform deformations. At the crosses, we detected bistability. (c) Phase diagram in low  $G$  regime obtained from numerical simulations of continuum model for the parameters of electronic supplementary material, figure S5b and comparison to the theoretical prediction equation (3.9) (solid line, which has slope  $-1$ ). (Online version in colour.)

Similarly, we can also select a solution for a given  $\epsilon$  and study how varying  $G$  impacts its total energy. Since we do not perturb the solution, it will remain trapped in the local minimum. We find that below a critical  $G$ , the energy difference between localized and uniform states becomes negative, i.e. the localized state has a lower energy compared to the uniform solution (figure 3e). The critical  $G$  increases for increasing  $\epsilon$ , hence expanding the window of values for shear modulus for which we can expect to find localized states.

#### (d) Phase diagram for localized deformations

Our analysis implies that localized deformations are stable solutions for intermediate values of shear modulus  $G$  (figure 4). By analysing the energy of uniform and localized solutions, we found that decreasing  $G$  from the  $G \rightarrow \infty$  limit below a critical value  $G^{crit}$  causes localized deformations to have a lower total energy than the homogeneous buckled solution. This critical value is given by (see electronic supplementary material, S3.7)

$$\left(\frac{G}{K}\right)^{crit} \propto \epsilon - \epsilon^*; \quad (3.8)$$

it increases with increasing  $\epsilon$ . Moreover, our perturbative solution, equation (3.5), valid for low  $G$ , shows that, in this limit, decreasing  $G$  causes the width  $w$  of localization to increase; eventually, localization disappears when  $w$  approaches system size  $L$ ; using equation (3.6), we find that this occurs below

$$\left(\frac{G}{K}\right)^* \propto (\epsilon - \epsilon^*)^{-1} \left(\frac{\lambda}{L}\right)^4. \quad (3.9)$$

These two effects give rise to the phase diagram in figure 4a, where localized deformations emerge for intermediate values of  $G$ . We have verified these relationships using computer simulations both in the high  $G$  (figure 4b) and low  $G$  regimes (figure 4c).

We note that our system displays bistability. If we prepare the homogeneous state at  $G = 0.001$ , which is well below the value at which only localized solutions exist (figure 4b), we find that small perturbations of the filament relax back to the homogeneous state, while large amplitude perturbations can persist as localized solutions.



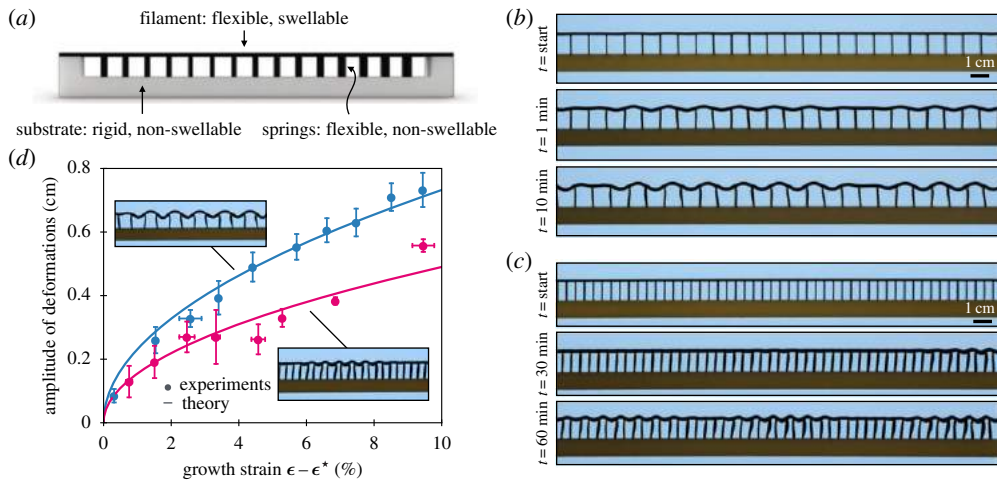


**Figure 5.** Experimental realization of geometric localization using 3D printing. (a) Schematic of the experimental realization of the system using a multi-material 3D-printed plastic model for the growth of a filament attached to a shearable substrate. The ends of the flexible filament are clamped. (b,c) Images of swelling 3D-printed samples placed in isopropyl alcohol showing the development of localized deformations over time: the number of vertical springs is  $n_s = 28$  (b), and  $n_s = 56$  (c). The different spacing between ‘springs’ allows us to control the mechanical parameters  $G, K, S$ , hence the form of localized deformations. Scale bar, 1 cm. (d) Measured amplitude of deformations for the samples in (b,c) as a function of growth strain  $\epsilon - \epsilon^*$  is compared to theory, equation (3.7) (solid line). (Online version in colour.)

## 4. Experiments

Using a Connex500 multi-material 3D printer (Stratasys, Eden Prairie, MN), we constructed a simple experimental realization of a growing filament bound to a shearable substrate to assess the occurrence of localized deformations (figure 5a). The 3D-printed samples consisted of three parts: (i) a rigid, non-swellable substrate, (ii) a flexible and swellable ‘filament’ and (iii) a series of flexible and non-swellable ‘springs’ connecting the filament to the substrate [22]. During the fabrication process, a photosensitive liquid precursor (the 3D printer ink) is deposited in a voxel-by-voxel fashion. Several precursors are used to print multiple materials with different properties and the resulting modulus can be tuned by varying the concentration of photo-initiator. A UV light cross-links the liquid precursors in a layer-by-layer fashion and this process is repeated until the full 3D model is built. Depending on the liquid precursor composition and the degree of cross-linking, a broad range of mechanical properties can be achieved from stiff thermoplastic-like to soft rubber-like materials. The degree of cross-linking also directly influences the swelling capacity of the polymer, and for the experiments described here, the component formulations were guided by previous formulations developed by Guiducci *et al.* [22]. Growth of the filament is induced through swelling by submerging the sample in isopropyl alcohol, and the sample deformations were filmed over 1 h with a digital camera. The structures were elevated off the bottom of the container to ensure that no flexible component was in direct contact with the walls, which would cause friction effects that could limit the motion of the filament or the springs. The swelling experiments were conducted on two different geometries with the same filament length  $L$ , but consisting of  $n_s = 28$  and  $n_s = 56$  vertical springs (figure 5b,c), i.e. the spacing  $b$  between springs is changed by a factor of 2 between the two experimental realizations. In both cases,  $b$  was sufficiently large to avoid differences in solvent diffusion between the two samples. Since the material properties as well as thickness of all components were identical for both realizations, changing  $b$  allows us to control the stretching modulus of the filament,  $S = \bar{S}b$ , as well as the stretching and shear moduli of the springs,  $K = \bar{K}/b^2$  and  $G = \bar{G}/(h_0^2 b)$ , while keeping the other parameters unchanged. According to our theory, the width, wavelength and amplitude

of localized deformations scale as  $w \propto G^{-1/4}$ ,  $\lambda \propto K^{-1/4}$  and  $A \propto (G/K)^{1/4}$ ; hence, we predict that reducing  $b$  results in localized deformations with overall smaller width, wavelength and amplitude. These predictions agree with the experimental observations (figure 5b,c). Moreover, the critical strain for the onset of deformations scales as  $\epsilon^* = \sqrt{BK/S}$ ; hence decreasing the spacing  $b$  between springs is expected to increase  $\epsilon^*$ . This prediction is consistent with the experimental observation that sample (c) requires a longer time for the onset of localized deformations compared to (b). For both geometries, we measured the amplitude of deformations as a function of excess growth strain  $\epsilon - \epsilon^*$  and verified the square-root scaling of the bifurcation predicted by equation (3.7) (figure 5d).

## 5. Discussion

We have described and studied a minimal realization of spatially localized deformations in a growing filament connected to a shearable substrate using a discrete rod model, a continuum theory, and implemented the results using experiments using a multi-material 3D printing framework. Our main results take the form of scaling relationships for key parameters relating to localized deformations, such as amplitude, wavelength and width, and a phase diagram for uniform and localized deformations. These can be particularly useful as guiding principles for designing controlled deformations with potential applications to mechanical memories. Indeed, our work shows that the ability to achieve localized deformations in filaments bound to shearable substrates depends on specific combinations of the mechanical parameters and the size of the system. Upon appropriate rescaling using the scaling relationships derived in this study, localized deformations could be appropriately designed both at the macro- and micro-scales.

Our work complements the literature in the field of spatially-dependent nonlinear dynamics, which suggested the possibility of localized deformations, either in purely theoretical systems [14–16] or in a variety of non-equilibrium settings [23–27]. Here, we have shown a simple physical realization of localized deformations in a one-dimensional equilibrium mechanical setting, obtained by exploiting substrate elasticity, simplifying further earlier work by us in two-dimensional mechanical settings [17]. Our work also provides an example of how to employ multi-material 3D printing as a reproducible, rapid and easily realizable method for studying complex problems related to multiscale mechanically constrained growth. In particular, the ability to control the deposition of material with very high resolution to create complex 3D structures might thus provide a practical research platform for investigating mechanical feedback on growth under different conditions, e.g. in the presence of gradients in strain or material properties. By incorporating extensions to two-dimensional (2D) systems, our approach could move us one step closer to understanding the two way-feedback between mechanics and growth/swelling kinetics, which is a defining feature in the growth of spatially extended structures in both materials science and biology.

We close by noting that our work applies in the limit when the filament and the substrate are idealized one-dimensional systems ( $a_1, a_2 \ll L$ , where  $a_1$  and  $a_2$  are the thickness and height of the filament). In the case of thin films/substrates ( $a_1 \ll a_2 \ll L$ ) or 2D systems ( $a_1 \ll a_2, L$ ), however, localized deformations caused by lateral forces may yield more complex 2D patterns. Extending our model to such situations will require accounting for the role of substrate nonlinearities on the stability of localized deformations [28–31], with the film modelled by nonlinear plate theory [32].

**Data accessibility.** This article does not contain any additional data.

**Authors' contributions.** T.C.T.M. and R.K. contributed equally to this work. R.K. and C.S. performed numerical simulations. T.C.T.M., A.J.D. and L.M. developed the mathematical analysis. T.C.T.M. and J.C.W. performed the experiments. T.C.T.M., R.K. and L.M. wrote the paper, with input from the other authors. L.M. conceived of research, formulated the mathematical models, designed the experiments and supervised the work.

**Competing interests.** We declare we have no competing interests.

**Funding.** We acknowledge financial support from the Swiss National Science foundation (T.C.T.M.), the Netherlands Organization for Scientific Research (NWO-FOM) within the program 'Barriers in the Brain: the Molecular Physics of Learning and Memory' (no. FOM-E1012M, R.K. and C.S.), the Schiff Foundation and

## References

1. Winkler E. 1867 *Die Lehre von der Elastizität und Festigkeit*. Prague, Czech Republic: Dominicus.
2. Diamant H, Witten TA. 2011 Compression induced folding of a sheet: an integrable system. *Phys. Rev. Lett.* **107**, 164302. (doi:10.1103/PhysRevLett.107.164302)
3. Yoo PJ, Lee HH. 2008 Complex pattern formation by adhesion-controlled anisotropic wrinkling. *Langmuir* **24**, 6897–6902. (doi:10.1021/la800126r)
4. Brau F, Damman P, Diamant H, Witten TA. 2013 Wrinkle to fold transition: influence of the substrate response. *Soft Matter* **9**, 8177–8186. (doi:10.1039/c3sm50655j)
5. Pocivavsek L, Dellsy R, Kern A, Johnson S, Lin B, Lee KYC, Cerda E. 2008 Stress and fold localization in thin elastic membranes. *Science* **320**, 912–916. (doi:10.1126/science.1154069)
6. Hunt GW, Peletier MA, Champneys AR, Woods PD, Wade MA, Budd CJ, Lord G. 2000 Cellular buckling in long structures. *Nonlinear Dyn.* **21**, 3–29. (doi:10.1023/A:1008398006403)
7. Hunt GW, Wade MA. 1998 Localization and mode interaction in sandwich structures. *Proc. R. Soc. Lond. A* **454**, 1197–1216. (doi:10.1098/rspa.1998.0202)
8. Hohlfeld E, Mahadevan L. 2011 Unfolding the sulcus. *Phys. Rev. Lett.* **106**, 105702. (doi:10.1103/PhysRevLett.106.105702)
9. Cao Y, Hutchinson JW. 2012 Wrinkling phenomena in neo-Hookean film/substrate bilayers. *J. Appl. Mech.* **79**, 031019. (doi:10.1115/1.4005960)
10. Takei A, Jin L, Hutchinson JW, Fujita H. 2014 Ridge localizations and networks in thin films compressed by the incremental release of a large equibiaxial pre-stretch in the substrate. *Adv. Mater.* **26**, 4061–4067. (doi:10.1002/adma.201306162)
11. Jin L, Takei A, Hutchinson JW. 2015 Mechanics of wrinkle/ridge transitions in thin film/substrate systems. *J. Mech. Phys. Solids* **81**, 22–40. (doi:10.1016/j.jmps.2015.04.016)
12. Auguste A, Jin L, Suo Z, Hayward RC. 2014 The role of substrate pre-stretch in post-wrinkling bifurcations. *Soft Matter* **10**, 6520–6529. (doi:10.1039/C4SM01038H)
13. Knobloch E. 2015 Spatial localization in dissipative systems. *Annu. Rev. Condens. Matter Phys.* **6**, 325–359. (doi:10.1146/annurev-conmatphys-031214-014514)
14. Pomeau Y. 1986 Front motion, metastability and subcritical bifurcations in hydrodynamics. *Physica D* **23**, 3–11. (doi:10.1016/0167-2789(86)90104-1)
15. Couillet P, Riera C, Tresser C. 2000 Stable static localized structures in one dimension. *Phys. Rev. Lett.* **84**, 3069–3072. (doi:10.1103/PhysRevLett.84.3069)
16. Couillet P, Riera C, Tresser C. 2004 A new approach to data storage using localized structures. *Chaos* **14**, 193–198. (doi:10.1063/1.1642311)
17. Chung JY, Vaziri A, Mahadevan L. 2018 Reprogrammable Braille on an elastic shell. *Proc. Natl Acad. Sci. USA* **115**, 7509–7514. (doi:10.1073/pnas.1722342115)
18. Drazin PG. 2002 *Introduction to hydrodynamic stability*. Cambridge, UK: Cambridge University Press.
19. Cerda E, Mahadevan L. 2003 Geometry and physics of wrinkling. *Phys. Rev. Lett.* **90**, 074302. (doi:10.1103/PhysRevLett.90.074302)
20. Abramowitz LD, Lifshitz EM. 1970 *Theory of elasticity*. Oxford, UK: Pergamon Press.
21. Abramowitz M, Stegun IA. 1965 *Handbook of mathematical functions with formulas, graphs, and mathematical tables*. New York, NY: Dover.
22. Guiducci L, Weaver JC, Bréchet YJM, Fratzl P, Dunlop JWC. 2015 The geometric design and fabrication of actuating cellular structures. *Adv. Mater. Interfaces* **2**, 1500011. (doi:10.1002/admi.201500011)
23. Swift J, Hohenberg PC. 1977 Hydrodynamic fluctuations at the convective instability. *Phys. Rev. A* **15**, 319–328. (doi:10.1103/PhysRevA.15.319)
24. Cross MC, Hohenberg PC. 1993 Pattern formation outside of equilibrium. *Rev. Mod. Phys.* **65**, 851. (doi:10.1103/RevModPhys.65.851)
25. diBernardo M, Budd CJ, Champneys AR, Kowalczyk P. 2008 Qualitative theory of non-smooth dynamical systems. *Appl. Math. Sci.* **163**, 47–119. (doi:10.1007/978-1-84628-708-4\_2)
26. Devaney RL. 1977 Blue sky catastrophes in reversible and Hamiltonian systems. *Indiana Univ. Math. J.* **26**, 247–263. (doi:10.1512/iumj.1977.26.26018)

27. Lee KJ, McCormick WD, Ouyang Q, Swinney HL. 1993 Pattern formation by interacting chemical fronts. *Science* **261**, 192–194. (doi:10.1126/science.261.5118.192)
28. Allen HG. 1969 *Analysis and design of sandwich panels*. New York, NY: Pergamon Press.
29. Zang J, Zhao X, Cao Y, Hutchinson JW. 2012 Localized ridge wrinkling of stiff films on compliant substrates. *J. Mech. Phys. Solids* **60**, 1265–1279. (doi:10.1016/j.jmps.2012.03.009)
30. Sun J-Y, Xia S, Moon M-Y, Oh KH, Kim K-S. 2012 Folding wrinkles of a thin stiff layer on a soft substrate. *Proc. R. Soc. A* **468**, 932–953. (doi:10.1098/rspa.2011.0567)
31. Hutchinson JW. 2013 The role of nonlinear substrate elasticity in the wrinkling of thin films. *Phil. Trans. R. Soc. A* **371**, 20120422. (doi:10.1098/rsta.2012.0422)
32. Timoshenko S, Woinowsky-Krieger S. 1959 *Theory of plates and shells*. New York, NY: McGraw-Hill.

# Supplementary Information for

## Geometric localization in supported elastic struts

Thomas C. T. Michaels, R. Kusters, C. Storm, A.J. Dear, J.C. Weaver, L. Mahadevan

L Mahadevan.

E-mail: [lmahadev@g.harvard.edu](mailto:lmahadev@g.harvard.edu)

### Contents

<b>S1 Mapping the discrete rod model to the continuous equations</b>	<b>2</b>
S1.1 Stretching energy of filament . . . . .	2
S1.2 Stretching energy of substrate (springs) . . . . .	2
S1.3 Shear energy of substrate . . . . .	3
S1.4 Bending energy of filament . . . . .	3
S1.5 Total elastic energy in continuum limit . . . . .	3
S1.6 Euler-Lagrange equations . . . . .	3
<b>S2 Numerical analysis of localized deformations</b>	<b>4</b>
S2.1 Discrete rod model . . . . .	4
S2.1.1 Effect of growth and filament size on localization . . . . .	4
S2.1.2 Higher-order filament deformations . . . . .	4
S2.1.3 Edge buckling . . . . .	4
S2.2 Numerical evaluation of continuum limit equations using shooting algorithm . . . . .	5
<b>S3 Asymptotic analysis of continuum equations</b>	<b>5</b>
S3.1 Analysis of linearized equations . . . . .	7
S3.2 Uniform wrinkling solution for large shear modulus . . . . .	7
S3.3 Uniform wrinkling solution for low shear modulus . . . . .	7
S3.4 Energy contributions for uniform deformation . . . . .	7
S3.5 Rescaled Euler-Lagrange equations . . . . .	8
S3.6 Weakly non-linear perturbation . . . . .	9
S3.7 Energy scalings for localized solution . . . . .	10
S3.7.1 Shear energy . . . . .	10
S3.7.2 Filament stretching energy . . . . .	10
S3.7.3 Filament bending and spring energies . . . . .	11

## S1. Mapping the discrete rod model to the continuous equations

In this section, we outline the conversion from the discrete rod model (Eq. (1) of the main text) to the set of differential equations describing the continuous rod model (Eq. (2) of the main text). The total energy of the system in the discrete rod model (Eq. (1) of the main text) consists of four contributions: (i) the stretching energy of the filament ( $\mathcal{E}_S$ ), (ii) the stretching of the substrate ( $\mathcal{E}_K$ ), (iii) the shear energy of the filament ( $\mathcal{E}_G$ ), and (iv) the bending energy of the filament ( $\mathcal{E}_B$ ). Without loss of generality, we consider the case when  $n_s = N$ , hence  $\ell_0 = b$ .

In going from the discrete to the continuous limit, we replace the discrete index  $n$  by the continuous variable  $x = nb$  and let  $b \rightarrow 0$ , while keeping the total length of the filament  $L = Nb$  constant. Discrete horizontal  $U_n$  and vertical  $W_n$  displacements are replaced by continuous fields  $U(x)$  and  $W(x)$ . Finite differences are replaced with continuous derivatives up to second order in  $b$ , e.g.

$$\begin{aligned}
 U_{n-1} - U_n &\rightarrow U(x-b) - U(x) \\
 &\simeq -bU'(x) + \frac{b^2}{2}U''(x) + \dots \\
 U_{n+1} - U_n &\rightarrow U(x+b) - U(x) \\
 &\simeq bU'(x) + \frac{b^2}{2}U''(x) + \dots \\
 W_{n-1} - W_n &\rightarrow W(x-b) - W(x) \\
 &\simeq -bW'(x) + \frac{b^2}{2}W''(x) + \dots \\
 W_{n+1} - W_n &\rightarrow W(x+b) - W(x) \\
 &\simeq bW'(x) + \frac{b^2}{2}W''(x) + \dots \\
 W_{n+1} + W_{n-1} - 2W_n &\rightarrow W(x+b) + W(x-b) - 2W(x) \\
 &\simeq b^2W''(x) + \dots
 \end{aligned} \tag{S1}$$

Finally, sums are replaced by integrals

$$\sum_n (\dots) \rightarrow \int_0^{L(1+\epsilon)} (\dots) \frac{dx}{b}. \tag{S2}$$

For clarity, we will use bars to denote elastic constants in the discrete limit. We now analyze each energy contribution separately.

**S1.1. Stretching energy of filament.** The energy related to the stretching of the filament is proportional to the square of the strain  $(\ell_n - \ell_0)/\ell_0$

$$\mathcal{E}_S = \frac{\bar{S}}{2\ell_0} \sum_{n=1}^{n_s} (\ell_n - \ell_0)^2, \tag{S3}$$

where, following growth,  $\ell_0 = b(1 + \epsilon)$ . Using Pythagoras theorem and Fig. S1, we have

$$\ell_n = \sqrt{(b - U_{n-1} + U_n)^2 + (W_n - W_{n-1})^2}. \tag{S4}$$

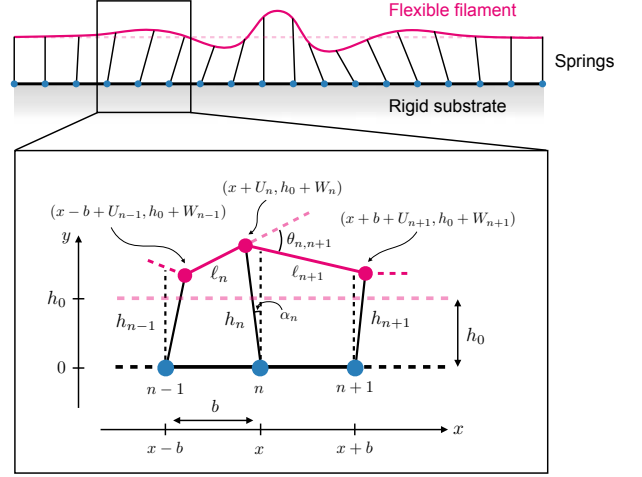


**Fig. S1.** Schematic representation of the discrete rod model for the transition to the continuous formulation for  $n_s = N$  and definition of the angles  $\alpha_n$  (shear) and  $\theta_{n,n+1}$  (bending).

Hence, with the replacement  $x = nb$ , and Eq. (S1), we find after keeping only the leading order terms:

$$\begin{aligned}
 \mathcal{E}_S &= \frac{\bar{S}}{2\ell_0} \sum_{n=1}^{n_s} \left[ \sqrt{(b - U_{n-1} + U_n)^2 + (W_n - W_{n-1})^2} - b(1 + \epsilon) \right]^2 \\
 &\rightarrow \frac{\bar{S}}{2\ell_0} \int_0^{L(1+\epsilon)} \left[ \sqrt{(b + bU'(x))^2 + (bW'(x))^2} - b(1 + \epsilon) \right]^2 \frac{dx}{b} \\
 &\simeq \frac{\bar{S}b^2}{2\ell_0} \int_0^{L(1+\epsilon)} \left[ \sqrt{1 + 2U'(x) + \dots + W'(x)^2} - (1 + \epsilon) \right]^2 \frac{dx}{b} \\
 &\simeq \frac{\bar{S}b}{2\ell_0} \int_0^{L(1+\epsilon)} \left[ U'(x) + \frac{W'(x)^2}{2} + \dots - \epsilon \right]^2 dx \\
 &=: \frac{S}{2} \int_0^{L(1+\epsilon)} \left[ U'(x) + \frac{W'(x)^2}{2} - \epsilon \right]^2 dx,
 \end{aligned} \tag{S5}$$

where in the second and third lines, we have used the expansion  $(1 + y)^\beta \simeq 1 + \beta y + \dots$  for  $y \ll 1$ . Hence, in the continuous limit we have

$$S = \frac{\bar{S}b}{\ell_0}. \tag{S6}$$

**S1.2. Stretching energy of substrate (springs).** The contribution attributed to the stretching of the substrate (springs) reads

$$\mathcal{E}_K = \frac{\bar{K}}{2b} \sum_{n=1}^N (h_n - h_0)^2, \tag{S7}$$

where  $h_0$  is the rest length of the springs and using Fig. S1,

$$h_n = \sqrt{U_n^2 + (h_0 + W_n)^2}. \tag{S8}$$



Keeping only the leading order term, we find (Fig. S1(a)):

$$\begin{aligned}
E_K &= \frac{\bar{K}}{2b} \sum_{n=1}^N \left[ \sqrt{U_n^2 + (h_0 + W_n)^2} - h_0 \right]^2 \\
&\rightarrow \frac{\bar{K}}{2b} \int_0^{L(1+\epsilon)} \left[ \sqrt{U(x)^2 + (h_0 + W(x))^2} - h_0 \right]^2 \frac{dx}{b} \\
&\simeq \frac{\bar{K}}{2b} \int_0^{L(1+\epsilon)} \left[ \sqrt{h_0^2 + 2h_0 W(x) + \dots} - h_0 \right]^2 \frac{dx}{b} \\
&\simeq \frac{\bar{K}}{2b^2} \int_0^{L(1+\epsilon)} W(x)^2 dx \\
&=: \frac{K}{2} \int_0^{L(1+\epsilon)} W(x)^2 dx,
\end{aligned} \tag{S9}$$

where, we have used again the expansion  $(1+y)^\beta \simeq 1 + \beta y + \dots$  for  $y \ll 1$ . In the continuous limit, we thus have

$$K = \frac{\bar{K}}{b^2}. \tag{S10}$$

**S1.3. Shear energy of substrate.** The shear contribution reads

$$\mathcal{E}_G = \frac{\bar{G}}{2} \sum_{n=1}^N \alpha_n^2, \tag{S11}$$

where the shear angle  $\alpha_n$  is defined in Fig. S1. Using simple geometry, we find

$$\begin{aligned}
\mathcal{E}_G &= \frac{\bar{G}}{2} \sum_{n=1}^N \left( \arctan \left[ \frac{U_n}{h_0 + W_n} \right] \right)^2 \\
&\rightarrow \frac{\bar{G}}{2} \int_0^{L(1+\epsilon)} \left( \arctan \left[ \frac{U(x)}{h_0 + W(x)} \right] \right)^2 \frac{dx}{b} \\
&\simeq \frac{\bar{G}}{2h_0^2 b} \int_0^{L(1+\epsilon)} U(x)^2 dx \\
&=: \frac{G}{2} \int_0^{L(1+\epsilon)} U(x)^2 dx,
\end{aligned} \tag{S12}$$

where, in the last step, we used the expansion  $\arctan(y) \simeq y + \dots$  for  $y \ll 1$ . In the continuous limit, we thus have:

$$G = \frac{\bar{G}}{h_0^2 b}. \tag{S13}$$

**S1.4. Bending energy of filament.** The bending energy reads

$$\mathcal{E}_B = \frac{\bar{B}}{\ell_0} \sum_{n=1}^N (1 - \cos \theta_{n,n+1}), \tag{S14}$$

where the bending angle  $\theta_{n,n+1}$ , which is defined in Fig. S1, is the angle formed by the tangent vectors of consecutive filament segments. This form of bending energy is valid for weak bending. In fact, the bending energy of an arc segment of a worm-like chain is given by  $\mathcal{E}_B = (2\bar{B})/\ell_0 \theta \sin(\theta/2)$ , which for small  $\theta$  reduces to  $(\bar{B}/\ell_0) \theta^2$ , which is approximately  $(\bar{B}/2\ell_0) (1 - \cos \theta)$ . For small deflections, we can expand to leading order  $1 - \cos \theta_{n,n+1} \simeq \theta_{n,n+1}^2/2$ . The angle  $\theta_{n,n+1}$  can be approximated as

$$\theta_{n,n+1} \simeq \frac{W_{n+1} - 2W_n + W_{n-1}}{b} \rightarrow bW''(x). \tag{S15}$$

Hence,

$$\begin{aligned}
\mathcal{E}_B &\simeq \frac{\bar{B}}{2\ell_0} \sum_{n=1}^N \theta_{n,n+1}^2 \rightarrow \frac{\bar{B}}{\ell_0} \int_0^{L(1+\epsilon)} (bW''(x))^2 \frac{dx}{b} \\
&=: \frac{B}{2} \int_0^{L(1+\epsilon)} W''(x)^2 dx.
\end{aligned} \tag{S16}$$

In the continuous limit, we thus have

$$B = \frac{\bar{B}b}{\ell_0}. \tag{S17}$$

**S1.5. Total elastic energy in continuous limit.** In summary, the elastic energy  $\mathcal{E}(s)$  in the continuous limit may be written as function of the arc length  $x$  to second order in the displacements  $U(x)$  and  $W(x)$  as:

$$\begin{aligned}
\mathcal{E} &= \int_0^{L(1+\epsilon)} \left( \frac{B}{2} W''(x)^2 + \frac{S}{2} \left[ U'(x) + \frac{W'(x)^2}{2} - \epsilon \right]^2 \right. \\
&\quad \left. + \frac{K}{2} W(x)^2 + \frac{G}{2} U(x)^2 \right) dx,
\end{aligned} \tag{S18}$$

which is Eq. (2) of the main text.

**S1.6. Euler-Lagrange equations.** Finally, we can write down the Euler-Lagrange equations for the energy functional  $\mathcal{E}(s)$ , Eq. (S18). This yields

$$\begin{aligned}
\frac{\delta \mathcal{E}}{\delta W(x)} &= \frac{\partial \mathcal{E}}{\partial W(x)} - \frac{d}{dx} \left( \frac{\partial \mathcal{E}}{\partial W'(x)} \right) + \frac{d^2}{dx^2} \left( \frac{\partial \mathcal{E}}{\partial W''(x)} \right) \\
&= KW(x) - S \left[ \left( U'(x) + \frac{W'(x)^2}{2} - \epsilon \right) W'(x) \right]' + BW''''(x) \\
&= KW(x) - S \left[ U'(x) + \frac{W'(x)^2}{2} - \epsilon \right] W''(x) \\
&\quad - S [U''(x) + W'(x)W''(x)] W'(x) + BW''''(x) = 0
\end{aligned} \tag{S19a}$$

and

$$\begin{aligned}
\frac{\delta \mathcal{E}}{\delta U(x)} &= \frac{\partial \mathcal{E}}{\partial U(x)} - \frac{d}{dx} \left( \frac{\partial \mathcal{E}}{\partial U'(x)} \right) \\
&= GU - S \left[ U'(x) + \frac{W'(x)^2}{2} - \epsilon \right]' \\
&= GU - S [U''(x) + W'(x)W''(x)] = 0.
\end{aligned} \tag{S19b}$$

By utilizing Eq. (S19b) in Eq. (S19a), we arrive at

$$\begin{aligned}
&BW''''(x) + S \left[ \epsilon - U'(x) - \frac{W'(x)^2}{2} \right] W''(x) \\
&\quad + KW(x) - GU(x)W'(x) = 0,
\end{aligned} \tag{S20a}$$

$$S [U''(x) + W'(x)W''(x)] = GU(x), \tag{S20b}$$

which are Eqs. (3) of the main text.

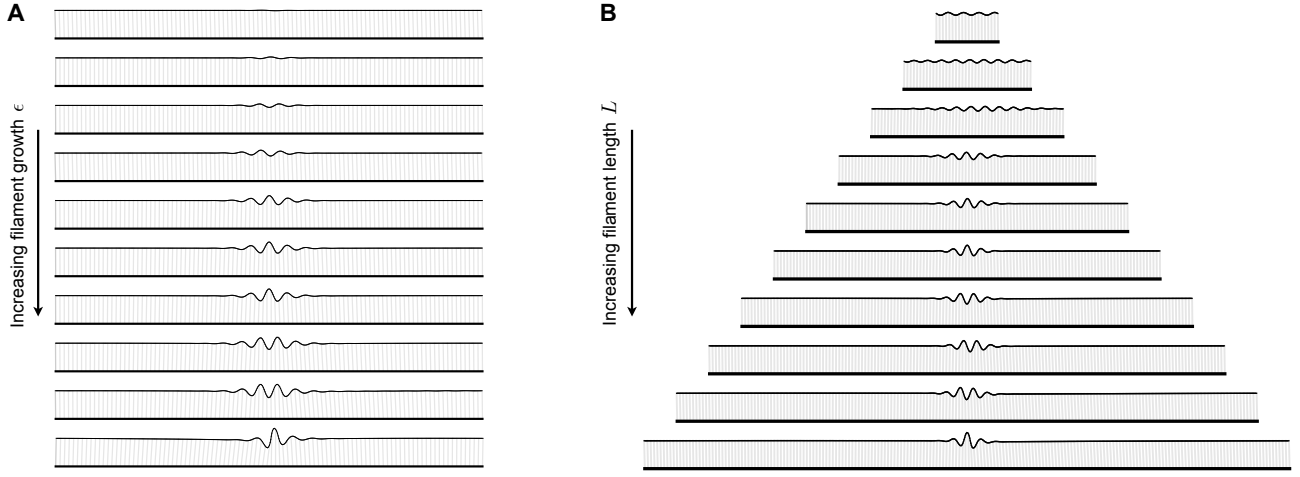


**Fig. S2.** (a) Shape of a filament with increasing growth calculated using the discrete rod model. From top to bottom:  $\epsilon = 0.05\%, 0.1\%, 0.15\%, 0.25\%, 0.5\%, 0.7\%, 0.8\%, 1\%, 1.25\%, 1.4\%$ . (b) Effect of increasing filament length on localization. From top to bottom:  $N = 20, 40, 60, 80, 100, 120, 140, 160, 180, 200$ .

## S2. Numerical analysis of localized deformations

**S2.1. Discrete rod model.** To minimize the total energy of the system  $\mathcal{E}$  in the discrete rod model (Eq. (1) of the main text), we either use Newton's method, present in the FindMinimum routine, or a global energy search present in the NMinimize routine. Both routines are implemented in Wolfram Mathematica. We note however, that the Newton's iteration method only guarantees a local minimum and that even with NMinimize we have no guarantee of finding the actual global minimum. Therefore care has to be taken in evaluating the growth. We are not necessarily interested in the global minimum of the system but in the solution that arises subsequent to growth of the filament. The procedure we use to "grow" the flexible filament is the following: we initiate a configuration where the springs are in their rest configuration and no bending is present in the filament. We then increase the rest length of the springs  $\ell_0$  that make up the rod with a small amount  $\ell_0\epsilon$  such that the new length of the segments  $\ell_0(1 + \epsilon)$ . We then use our minimisation algorithm to find the energetically optimal configuration of the filament. Since this system typically has multiple local minima, we will explore the different solution branches and calculate their energy and stability by adding white noise to the initial configuration. In particular, to map out these various branches as function the relevant parameters  $\bar{G}$  and  $\epsilon$ , we use a local conjugate gradient method to identify the various local energetic minima; then by gradually increasing/decreasing  $\bar{G}$  and  $\epsilon$  we can probe the various solution branches. To probe the stability of the various branches we apply a random perturbation (white noise) to the solutions and study how, depending on the amplitude, the solution relaxes back to the branch or finds another minimal energy solution.

**S2.1.1. Effect of growth and filament size on localization.** Using our discrete rod model, we studied numerically how growth induces localization and show this for a system of  $N = 100$  connecting springs ( $\bar{B} = 0.1$ ,  $\bar{K} = 0.1$  and  $\bar{G} = 0.1$ ) by simulating the shape of the filament as a function of growth  $\epsilon$  (Fig. S2(a)). We find that the width of the localized structure decreases upon increasing  $\epsilon$ . Another way to decrease the localization

length is to increase the size  $L$  of the system. In Fig. S2(b), we simulated the shape of the filament for various system sizes while keeping the relative amount of growth and the other parameters constant. While increasing the system size does not affect the wavelength of the perturbation, there is an effect of system size on the width of localization. This effect is captured by our analytical solution to the continuous equations (see Fig. S10).

**S2.1.2. Higher-order filament deformations.** In the main text, we have focussed only on the homogeneous and single localized buckling solutions. Using our discrete rod model, we can also examine other local energetic solutions; indeed, not unlike many systems governed by Swift-Hohenberg type equations (3), our system exhibits multiple stable and unstable spatially localized and uniform branches. In Fig. S3, we find that, besides the localized solution, the uniform solution as well as solutions with multiple bumps are stable solutions for finite shear modulus. In Fig. S3(b) we have plotted the total energy and the maximal vertical amplitude of the filament as a function of  $\epsilon$ . All the states were obtained with identical system parameters, but different random initial configurations and values of  $\epsilon$ . Once we picked up a branch we incrementally decrease/increase the amount of growth, using the previous solution as input until the solution jumps to another branch. This shows that, even while the shear field is not localized along the system solutions, for certain values of  $\bar{G}$  and  $\epsilon$  multiple bump solutions are stable solutions of the governing equations.

**S2.1.3. Edge buckling.** We also studied buckling of a growing filament attached to a solid filament, where the end-points of the filaments are free. For simplicity we only considered inextensible filaments here ( $\bar{S} = 1000\bar{K}$ ) with vanishing shear modulus  $\bar{G} = 0$ . As can be seen in Fig. S4(a) for a filament with  $N = 50$  during the initial growth the filament stretches parallel to the solid substrate. Above a critical extension  $\epsilon^*$ , the filaments starts to buckle at the edge. The exact value of  $\epsilon^*$  as well as the buckling wavelength  $\lambda$  strongly depend on the value of  $\bar{B}/\bar{K}$ . To enhance the stability of our minimization algorithm we minimize half of the space for the non-periodic

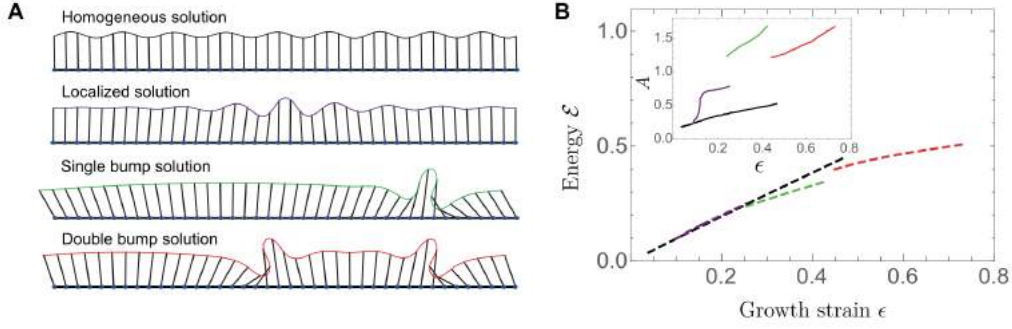


**Fig. S3.** (a) Homogeneous solution, symmetric localized solution, asymmetric single bump solution and double bump solution. Note that these branches occur and are stable at different values of growth  $\epsilon$ . (b) Energy and corresponding amplitude of the various branches. The colors correspond to the various solutions in (a) ( $N = 40$ ,  $\bar{S} = 100$ ,  $n_s = 157$ ,  $\bar{G} = 0.01$ ,  $\bar{B} = 0.4$ ,  $b = 2$  and  $\bar{K} = 0.1$ )

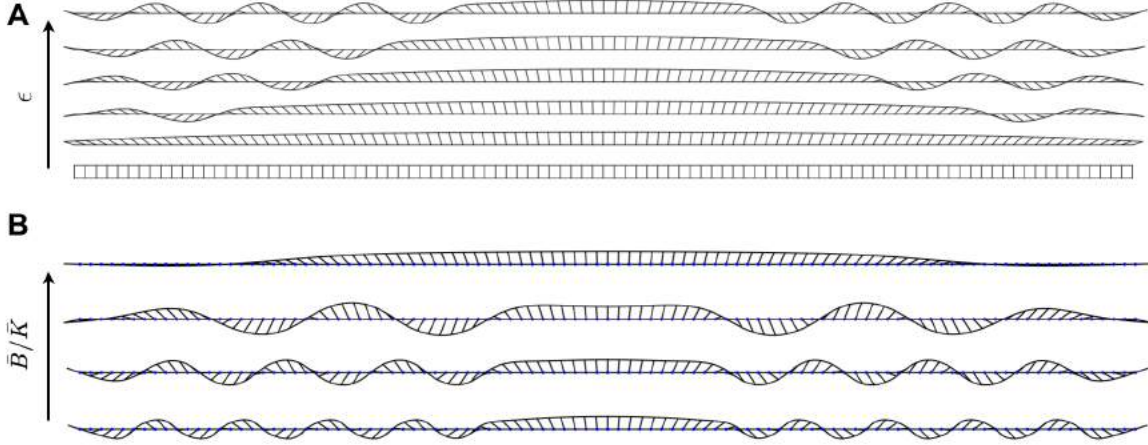


**Fig. S4.** (a) The equilibrium shape for a filament with free edges as function of growth  $\epsilon$ . (b) The equilibrium shape for a filament for various ratios of bending modulus and spring stiffness  $\bar{B}/\bar{K}$  from  $10^{-3}$  to 1 after a growth of  $\epsilon = 0.15$  for a system with  $N = 50$  springs.

filament. We assume that the minimal energy solution is symmetric around the midline of the system, this is achieved by fixing the  $x$ -position of the midpoint segment and equating the  $y$ -coordinate of the last two segments. We have verified that this approach yields the same equilibrium shape as when we would consider the whole space, at least for large systems. For small systems, the antisymmetric solutions are excluded by construction.

Fig. S4 (b) shows a filament that is adhered with 50 springs corresponding to an extension  $\epsilon = 0.15$ . Similar to what we observed for the buckling of a periodic filament we find that decreasing  $\bar{B}/\bar{K}$ , decreases the wave length of the edge buckling.

**S2.2. Numerical evaluation of continuous limit equations using shooting algorithm.** The Euler Lagrange equations Eq. (S20) are transformed into a set of 6 first order ODEs for  $w_0 = W$ ,  $w_1 = W'$ ,  $w_2 = W''$ ,  $w_3 = W'''$ ,  $u_0 = U$ ,  $u_1 = U'$ . This system of ODEs is solved using a shooting algorithm and once we find a solution branch we follow it by slightly perturbing our shooting parameters. These coupled nonlinear differential equations are typically hard to solve and, similarly to the discrete rod model, we cannot guarantee that the obtained solutions is the energetically most favourable one. To simplify this shooting algorithm we only consider the solution on the half-interval  $0 \leq x \leq L/2$ ; hence, we shoot

from the edge of the domain towards the centre of the domain and use the symmetry around  $x = 0$  to find the full solution (ensuring that  $U(L/2) = W'(L/2) = W'''(L/2) = 0$ ). Since coupled fourth order differential equations typically have a wealth of possible solutions, finding the right initial guesses for the shooting algorithm corresponding to a solution is not straightforward. However, close to the bifurcation point  $\epsilon^*$  we were able to obtain solutions that satisfied the boundary conditions. We show a set of these localized solutions obtained from numerical evaluation of the continuous Euler-Lagrange equations Eq. (S20) for various values of shear modulus  $G$  and growth strain  $\epsilon$  in Fig. S5. Note that the spatial extend of the localized solution, obtained from the continuous differential equations decreases upon increasing  $\epsilon$ , highly similar to what we found for the discrete rod model. Moreover, increasing the shear modulus  $G$ , decreases the width of the localized solution. Note that, close to  $\epsilon^*$ , we find higher order solutions, which are all different solution branches, not unlike those observed in the discrete rod model. A full analysis of the full parameter space, however, is out of the scope of this paper and is left for a future study.

### S3. Asymptotic analysis of continuous equations

In this section, we provide the mathematical details pertaining to the weakly non-linear analysis of continuous equations,

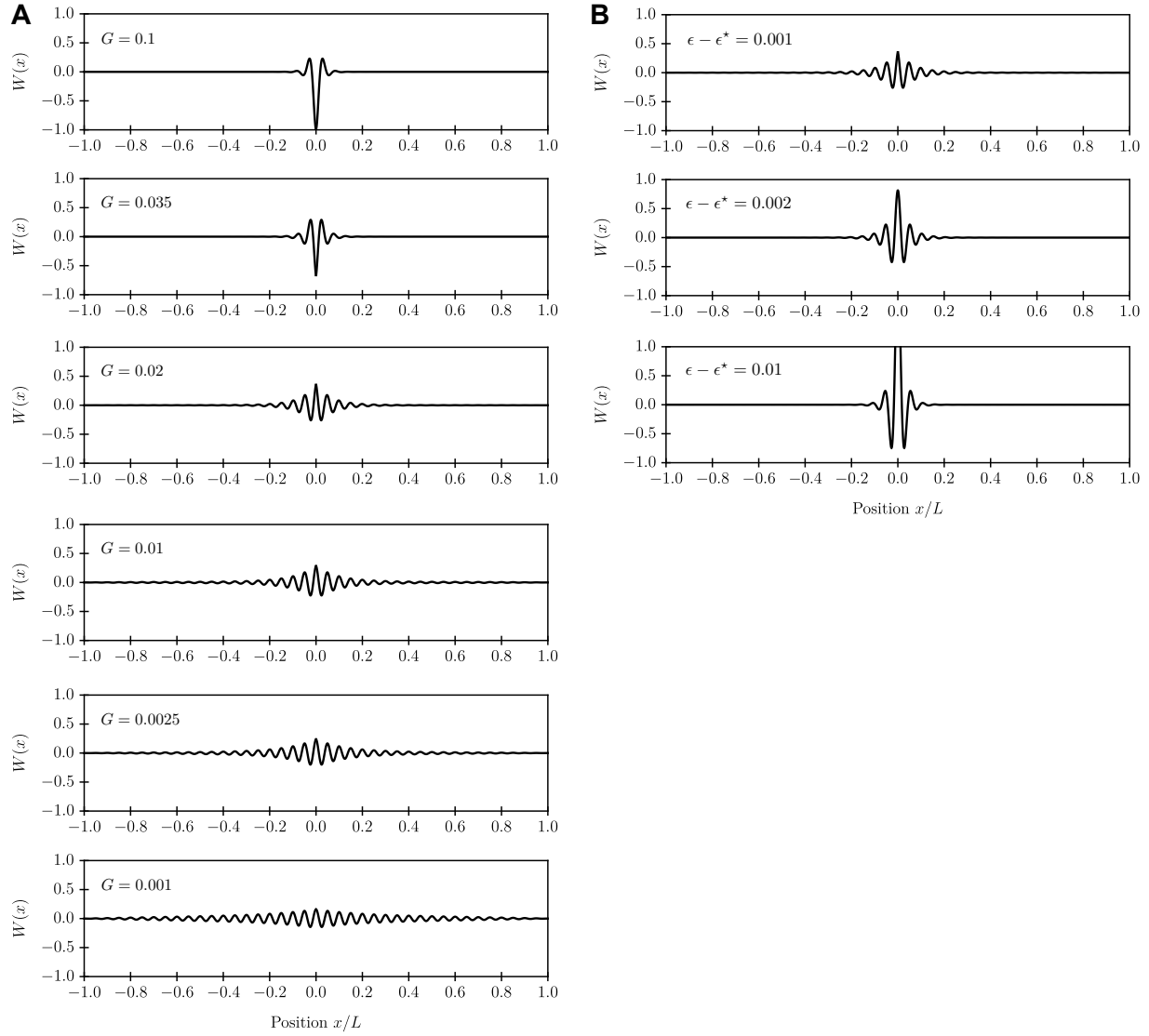


**Fig. S5.** Solutions for the vertical displacement  $W(x)$  from Eq. (S20a) and Eq. (S20b) for a system width width  $20 \times \lambda$  and for the following parameters: (a)  $K = 1$ ,  $B = 1$ ,  $S = 100$ ,  $\epsilon = 0.021$  and varying  $G$ ; (b)  $K = 1$ ,  $B = 1$ ,  $G = 0.01$  and varying  $\epsilon - \epsilon^*$ .

Eqs. (3) in the main text. We will solve these equations on the half-interval  $x \in [0, L/2]$  with the boundary conditions  $U(L/2) = W(L/2) = W'(L/2) = 0$  and  $U(0) = W'(0) = W'''(0) = 0$ .

**S3.1. Analysis of linearized equations.** The first step in this analysis is to consider the linearized Euler-Lagrange equations, which read

$$BW''''(x) + S\epsilon W''(x) + KW(x) = 0 \quad [\text{S21a}]$$

$$SU''(x) = GU(x) \quad [\text{S21b}]$$

subject to the boundary conditions  $U(L/2) = U(0) = W(L/2) = W'(L/2) = W'(0) = W'''(0) = 0$ . Eq. (S21b) has a general solution of the form  $U(x) = C_1 e^{\sqrt{G/S}x} + C_2 e^{-\sqrt{G/S}x}$ ; the boundary conditions necessarily imply  $C_1 = C_2 = 0$ , hence in the linear regime the horizontal displacement vanishes,  $U(x) \equiv 0$ . To solve equation Eq. (S21a) we make the Ansatz  $W = e^{\Omega x}$ , which yields

$$\lambda\Omega = \pm \sqrt{-\frac{S\epsilon}{2\sqrt{BK}} \pm \sqrt{\left(\frac{S\epsilon}{2\sqrt{BK}}\right)^2 - 1}}, \quad \lambda = \left(\frac{B}{K}\right)^{1/4}. \quad [\text{S22}]$$

From this equation we see that  $\Omega$  is purely imaginary when the argument of the inner square root is positive

$$\left(\frac{S\epsilon}{2\sqrt{BK}}\right)^2 - 1 > 0 \quad \Rightarrow \quad \epsilon > \epsilon^* = \frac{2\sqrt{BK}}{S}. \quad [\text{S23}]$$

When  $\epsilon < \epsilon^*$ ,  $\Omega$  has a real part; together with the boundary conditions, this implies  $W(x) \equiv 0$ . When  $\epsilon > \epsilon^*$ , we get periodic wrinkling, and a non-zero solution exists. Note that the bifurcation point  $\epsilon^*$ , which we have obtained from the linearized system, is the same for the non-linear system.

**S3.2. Uniform wrinkling solution for large shear modulus.** We pause our analysis here to discuss two special cases of particular interest: (i) the limit of large shear modulus  $G \rightarrow \infty$  and (ii) the limit of zero shear modulus  $G = 0$  (see Sec. S3.3). The limit  $G \rightarrow \infty$  recovers the classical Winkler foundation (2). In both limits, we find uniformly wrinkling solutions.

In particular, when  $G \rightarrow \infty$ , Eq. (S20b) implies  $U(x) \equiv 0$ , i.e. there is no shear field. Substituting this into Eq. (S20a) yields

$$BW''''(x) + S\left[\epsilon - \frac{W'(x)^2}{2}\right]W''(x) + KW(x) = 0. \quad [\text{S24}]$$

From the above analysis of the linearized equations, we know that strains smaller than  $\epsilon^*$  can be accommodated through filament stretching. Hence, we write  $\epsilon = (\epsilon - \epsilon^*) + \epsilon^*$  to yield

$$BW''''(x) + S\epsilon^*W''(x) + KW(x) + S\left[\epsilon - \epsilon^* - \frac{W'(x)^2}{2}\right]W''(x) = 0. \quad [\text{S25}]$$

Inextensibility of the filament beyond  $\epsilon^*$ , implies  $\epsilon - \epsilon^* - \frac{W'(x)^2}{2} \simeq 0$ ; hence,  $W(x)$  satisfies the linear equation  $BW''''(x) + S\epsilon^*W''(x) + KW(x) = 0$ , which has solution

$$W(x) = A \cos\left(\frac{x}{\lambda}\right), \quad \lambda = \left(\frac{B}{K}\right)^{1/4}. \quad [\text{S26}]$$

The constant of integration  $A$  can be determined from the inextensibility condition

$$\epsilon - \epsilon^* - \frac{W'(x)^2}{2} \simeq \epsilon - \epsilon^* - \frac{A^2}{2\lambda^2} \simeq 0 \quad \Rightarrow \quad A \simeq \sqrt{2(\epsilon - \epsilon^*)}\lambda. \quad [\text{S27}]$$

**S3.3. Uniform wrinkling solution for low shear modulus.** We now consider the opposite limit of vanishing shear modulus  $G = 0$ , which, as we will show here below, also yields a uniform wrinkling solution. When  $G = 0$ , Eq. (S20b) implies

$$U''(x) + W'(x)W''(x) = 0 \quad \Rightarrow \quad U'(x) + \frac{W'(x)^2}{2} = \text{const} \quad [\text{S28}]$$

Substituting this into Eq. (S20a) with  $G = 0$  yields

$$BW''''(x) + S\left[\epsilon - U'(x) - \frac{W'(x)^2}{2}\right]W''(x) + KW(x) = 0. \quad [\text{S29}]$$

Once again, the filament will be able to accommodate strain up until  $\epsilon^*$  through filament stretching. Writing  $\epsilon = (\epsilon - \epsilon^*) + \epsilon^*$  yields

$$BW''''(x) + S\epsilon^*W''(x) + KW(x) + S\left[\epsilon - \epsilon^* - U'(x) - \frac{W'(x)^2}{2}\right]W''(x) = 0. \quad [\text{S30}]$$

Inextensibility of the filament beyond  $\epsilon^*$ , implies  $\epsilon - \epsilon^* - U'(x) - \frac{W'(x)^2}{2} \simeq 0$ ; hence, we recover the uniform wrinkling regime

$$BW''''(x) + S\epsilon^*W''(x) + KW(x) = 0. \quad [\text{S31}]$$

In conclusion, the analysis of the limits  $G = 0$  and  $G \rightarrow \infty$  shows that in both cases there is no localization. Shear localization emerges for intermediate (but small) values of  $G$ .

**S3.4. Energy contributions for uniform deformation.** We now analyze the different contributions to elastic energy in the case of a uniform deformation. This analysis will be useful for comparing the elastic energies of localized and uniform deformations (see Sec. S3.7). We focus on the limit  $G \rightarrow \infty$ . In this case, the horizontal displacement field is zero,  $U = 0$ ; hence, the shear energy is zero and the total energy is associated with the stretching and bending of the filament and the vertical stretching of the springs. Up until  $\epsilon^*$ , the strain  $\epsilon$  is accommodated into stretching energy with  $U = W = 0$ ; the stretching energy reads therefore:

$$\mathcal{E}_S \simeq \begin{cases} \frac{S}{2}\epsilon^2 L & \text{for } \epsilon < \epsilon^* \\ \frac{S}{2}(\epsilon^*)^2 L & \text{for } \epsilon > \epsilon^* \end{cases} \quad [\text{S32}]$$

Accordingly, for  $\epsilon < \epsilon^*$  there is no bending or spring energy and the total energy constitutes only of the stretching energy. Above  $\epsilon^*$ , the stretching energy ceases to increase with  $\epsilon$  and the excess strain  $\epsilon - \epsilon^*$  is accommodated into bending and spring energy. The bending energy can thus be estimated as

$$\mathcal{E}_B = \frac{B}{2} \int_{-L/2}^{L/2} W''(x)^2 dx \simeq \frac{B}{2} \left(\frac{A}{\lambda^2}\right)^2 \frac{L}{2} \simeq \frac{\sqrt{BK}}{2} (\epsilon - \epsilon^*) L, \quad [\text{S33}]$$



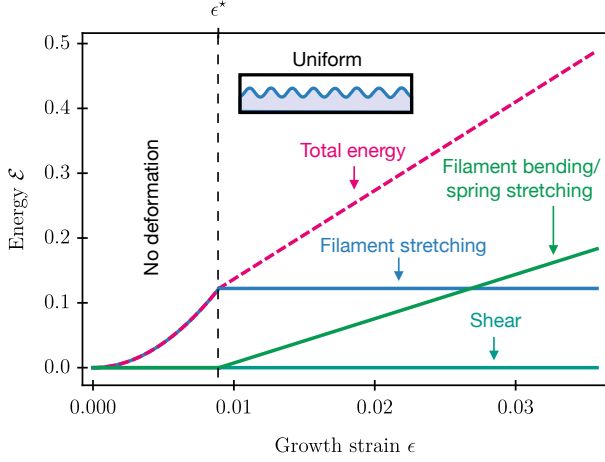


**Fig. S6.** Theoretical diagram illustrating the total, filament stretching, filament bending, spring stretching and shear energies as a function of strain  $\epsilon$  in the  $G \rightarrow \infty$  limit, Eq. (S37). Calculation parameters are:  $S = 10$ ,  $B = 0.2$ ,  $K = 0.01$ ,  $\epsilon = 9.5 \times 10^{-3}$ ,  $L = 23 \times \lambda$ . In this limit, there is no shear; the filament stretches until the bifurcation point  $\epsilon^*$ . Stretching energy becomes constant above  $\epsilon^*$  and excess strain  $\epsilon - \epsilon^*$  is accommodated as filament bending and spring stretching energy.

where we used that  $\int_{-L/2}^{L/2} \cos^2(x/\lambda) dx = \frac{L+\lambda \sin(x/\lambda)}{2} \simeq \frac{L}{2}$  for large  $L$ . Since  $\lambda = (B/K)^{1/4}$ , the same asymptotic result is obtained by considering the stretching energy of the springs

$$\begin{aligned} \mathcal{E}_K &= \frac{K}{2} \int_{-L/2}^{L/2} W(x)^2 dx \simeq KA^2 \frac{L}{2} \\ &\simeq B \frac{A^2}{\lambda^4} \frac{L}{2} \simeq \frac{\sqrt{BK}}{2} (\epsilon - \epsilon^*) L. \end{aligned} \quad [\text{S34}]$$

For  $\epsilon > \epsilon^*$ , the filament stretching energy is constant and can be re-written as

$$\mathcal{E}_S \simeq \frac{S}{2} (\epsilon^*)^2 L \simeq \sqrt{BK} \epsilon^* L. \quad [\text{S35}]$$

Thus, the total energy of the system for  $\epsilon > \epsilon^*$  is

$$\begin{aligned} \mathcal{E} &\simeq \mathcal{E}_S + \mathcal{E}_B + \mathcal{E}_K \\ &\simeq \sqrt{BK} \epsilon^* L + \frac{\sqrt{BK}}{2} (\epsilon - \epsilon^*) L + \frac{\sqrt{BK}}{2} (\epsilon - \epsilon^*) L \\ &= \sqrt{BK} \epsilon L. \end{aligned} \quad [\text{S36}]$$

Hence, the total energy of the system behaves as a function of  $\epsilon$  as (Fig. S6)

$$\mathcal{E} \simeq \begin{cases} \frac{S}{2} \epsilon^2 L & \text{for } \epsilon < \epsilon^* \\ \sqrt{BK} \epsilon L & \text{for } \epsilon > \epsilon^* \end{cases} \quad [\text{S37}]$$

It increases quadratically with  $\epsilon$  below the bifurcation point  $\epsilon^*$  and increases linearly with  $\epsilon$  for  $\epsilon > \epsilon^*$ .

**S3.5. Rescaled Euler-Lagrange equations.** We now turn our attention back to the solution of the Euler-Lagrange equations Eq. (S20) for a non-vanishing but small shear modulus  $G$ . In order to perform a weakly non-linear analysis of these equations, it is convenient to reformulate the problem in a way that the non-linear terms appear as a perturbation to the linearized theory. To so do, we first rewrite Eq. (S20) in dimensionless

form by rescaling  $x$ ,  $W$  and  $U$  by the characteristic length scale  $\lambda = (B/K)^{1/4}$  of the uniform periodic state

$$\bar{x} = \frac{x}{\lambda}, \quad \bar{W} = \frac{W}{\lambda}, \quad \bar{U} = \frac{U}{\lambda}. \quad [\text{S38}]$$

Doing so, we obtain the following rescaled Euler-Lagrange equations

$$\begin{aligned} \bar{W}''''(\bar{x}) + \sigma \left[ \epsilon - \bar{U}'(\bar{x}) - \frac{\bar{W}'(\bar{x})^2}{2} \right] \bar{W}''(\bar{x}) \\ + \bar{W}(\bar{x}) - \gamma \bar{U}(\bar{x}) \bar{W}'(\bar{x}) = 0, \\ \sigma (\bar{U}''(\bar{x}) + \bar{W}'(\bar{x}) \bar{W}''(\bar{x})) - \gamma \bar{U}(\bar{x}) = 0, \end{aligned} \quad [\text{S39a}]$$

where  $' = d/d\bar{x}$  and we have introduced the parameters

$$\sigma = \frac{S}{\sqrt{BK}}, \quad \gamma = \frac{G}{K} \quad [\text{S40}]$$

which represent rescaled stretching and shear moduli. We then write  $\epsilon = (\epsilon - \epsilon^*) + \epsilon^*$  to consider deviations from the bifurcation point  $\epsilon^*$ ; using  $\sigma \epsilon^* = 2$ , we obtain

$$\begin{aligned} \bar{W}''''(\bar{x}) + 2\bar{W}''(\bar{x}) + \bar{W}(\bar{x}) \\ + \sigma \left[ (\epsilon - \epsilon^*) - \bar{U}'(\bar{x}) - \frac{\bar{W}'(\bar{x})^2}{2} \right] \bar{W}''(\bar{x}) - \gamma \bar{U}(\bar{x}) \bar{W}'(\bar{x}) = 0, \\ \sigma (\bar{U}''(\bar{x}) + \bar{W}'(\bar{x}) \bar{W}''(\bar{x})) - \gamma \bar{U}(\bar{x}) = 0, \end{aligned}$$

This form of the continuous equations suggests considering  $\epsilon - \epsilon^*$  as a small perturbation parameter (the exact form of the relevant perturbation parameter in the problem will be determined below); to achieve this goal, we introduce the following rescalings of the vertical and horizontal displacement fields  $\bar{W}$  and  $\bar{U}$ :

$$\bar{W} = \sqrt{\epsilon - \epsilon^*} \bar{W}, \quad \bar{U} = (\epsilon - \epsilon^*) \bar{U}, \quad [\text{S42}]$$

i.e.

$$W = \lambda \sqrt{\epsilon - \epsilon^*} \bar{W}, \quad U = \lambda (\epsilon - \epsilon^*) \bar{U}. \quad [\text{S43}]$$

This transformation yields Eq. (5) of the main text

$$\begin{aligned} \bar{W}''''(\bar{x}) + 2\bar{W}''(\bar{x}) + \bar{W}(\bar{x}) + \sigma(\epsilon - \epsilon^*) \left[ \bar{W}''(\bar{x}) - \bar{U}'(\bar{x}) \bar{W}'(\bar{x}) \right. \\ \left. - \frac{\bar{W}'(\bar{x})^2}{2} \bar{W}''(\bar{x}) - \frac{\gamma}{\sigma} \bar{U}(\bar{x}) \bar{W}'(\bar{x}) \right] = 0 \end{aligned} \quad [\text{S44a}]$$

$$\bar{U}''(\bar{x}) + \bar{W}'(\bar{x}) \bar{W}''(\bar{x}) - \frac{\gamma}{\sigma} \bar{U}(\bar{x}) = 0. \quad [\text{S44b}]$$

Eq. (S44a) is particularly convenient, since it appears as the sum of the linear part and  $\sigma(\epsilon - \epsilon^*)$  times all non-linear terms.

To continue, we notice that the situation of interest is when  $\alpha = \gamma/\sigma \ll 1$ . This suggests solving Eq. (S44b) perturbatively in  $\alpha$ , by seeking a perturbation solution of the form

$$\bar{U} = \bar{U}_0 + \alpha \bar{U}_1 + \dots \quad [\text{S45}]$$

with the boundary conditions  $\bar{U}(\bar{L}/2) = 0$  and  $\bar{U}'(\bar{L}/2) = 1$ , where  $\bar{L} = L/\lambda$ . At first order in  $\alpha$ , we find:

$$\bar{U}' + \frac{(\bar{W}')^2}{2} = 1 + \alpha \frac{(\bar{x} - \bar{L}/2)^2}{2} + \dots \quad [\text{S46}]$$

The accuracy of the perturbative expansion Eq. (S46) against numerical solution of Eq. (S20) is discussed in Fig. S8(b). Note that Eq. (S46) implies that, in the presence of localization,



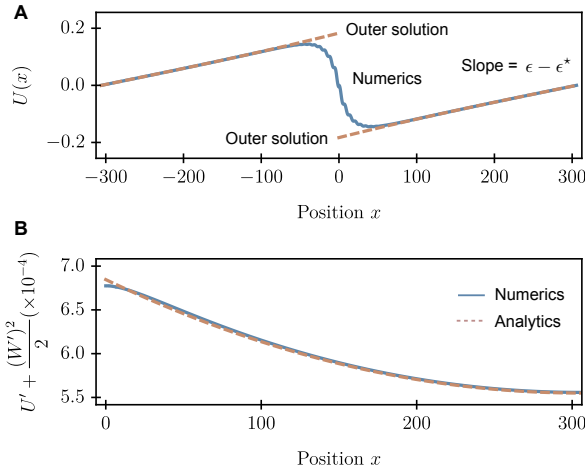


**Fig. S7.** (a) Comparison between numerical solution (solid line) for horizontal displacement  $U$  and the perturbative outer solution Eq. (S47) (dashed line). (b) Comparison between numerical solution (solid line) and perturbative expansion (dashed line) for  $U' + (W')^2/2$ , Eq. (S46). The parameters are:  $S = 10$ ,  $B = 0.2$ ,  $K = 0.01$ ,  $G = 5 \times 10^{-5}$ ,  $\epsilon = 9.5 \times 10^{-3}$ ,  $L = 23 \times \lambda$ .

there is a conversion of filament stretching energy into substrate shear energy (see Sec. S3.7). Note also that, away from the localized deformation, this perturbation Eq. (S46) corresponds to the outer solution for the horizontal displacement (see Fig. S8(a)):

$$\bar{U} = (\bar{x} - \bar{L}/2) + \alpha \frac{(\bar{x} - \bar{L}/2)^3}{6} + \dots, \quad [\text{S47}]$$

corrected by the term  $-(\bar{W}')^2/2$ .

We obtain the outer expansion solution for  $\bar{U}$  as follows: outside of the localization region, we can neglect terms associated with vertical displacement  $\bar{W}$ . hence, from Eq. (S44b) we obtain  $\bar{U}''(\bar{x}) = \frac{\gamma}{\sigma} \bar{U}(\bar{x})$ , which has the solution

$$\bar{U} = \frac{\sinh[\sqrt{\alpha}(\bar{x} - \bar{L}/2)]}{\sqrt{\alpha}}, \quad [\text{S48}]$$

which can be expanded in power series to yield Eq. (S47)

$$\bar{U} = \frac{\sinh[\sqrt{\alpha}(\bar{x} - \bar{L}/2)]}{\sqrt{\alpha}} = (\bar{x} - \bar{L}/2) + \alpha \frac{(\bar{x} - \bar{L}/2)^3}{6} + \dots, \quad [\text{S49}]$$

From this solution, we obtain the following approximation for the filament tension

$$\bar{U}' + \frac{(\bar{W}')^2}{2} = \cosh[\sqrt{\alpha}(\bar{x} - \bar{L}/2)] = 1 + \alpha \frac{(\bar{x} - \bar{L}/2)^2}{2} + \dots \quad [\text{S50}]$$

Combining Eq. (S46) with Eq. (S44a) (and keeping only the leading order terms in  $\alpha = \gamma/\sigma$ ), we arrive at:<sup>\*</sup>

$$\bar{W}'''' + 2\bar{W}'' + \bar{W} - \gamma(\epsilon - \epsilon^*) \frac{(\bar{x} - \bar{L}/2)^2}{2} \bar{W}'' = 0 \quad [\text{S53}]$$

<sup>\*</sup>Note that in deriving Eq. (S53), we neglected the contribution coming from the term  $\frac{\gamma}{\sigma} \bar{U}(\bar{x}) \bar{W}'(\bar{x})$  in Eq. (S44a). The full expression for Eq. (S53) is:

$$\bar{W}'''' + 2\bar{W}'' + \bar{W} - \gamma(\epsilon - \epsilon^*) \frac{(\bar{x} - \bar{L}/2)^2}{2} \bar{W}'' - \gamma(\epsilon - \epsilon^*)(\bar{x} - \bar{L}/2) \bar{W}' = 0 \quad [\text{S51}]$$

The difference between Eq. (S51) and Eq. (S53) is the term proportional to  $\bar{W}'$ . We now argue that this term can be neglected in front of the other ones. This can be seen as follows: introducing  $\delta = \gamma(\epsilon - \epsilon^*)$ ,  $X = \delta^{1/4}$  and  $X_e = \delta^{1/4}L/2$ , as in Eq. (S57), we can

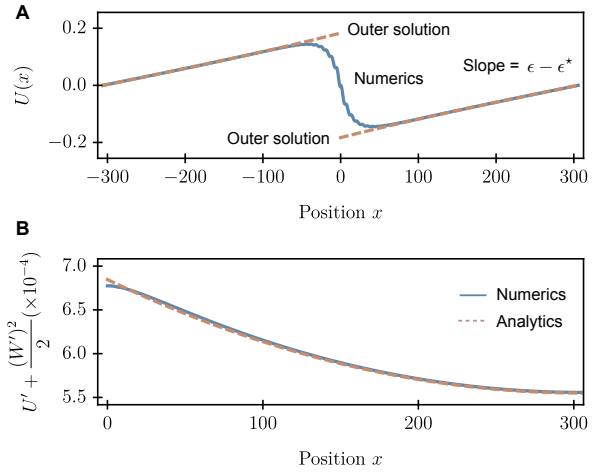


**Fig. S8.** (a) Comparison between numerical solution (solid line) for horizontal displacement  $U$  and the perturbative outer solution Eq. (S47) (dashed line). (b) Comparison between numerical solution (solid line) and perturbative expansion (dashed line) for  $U' + (W')^2/2$ , Eq. (S46). The parameters are:  $S = 10$ ,  $B = 0.2$ ,  $K = 0.01$ ,  $G = 5 \times 10^{-5}$ ,  $\epsilon = 9.5 \times 10^{-3}$ ,  $L = 23 \times \lambda$ .

which is Eq. (6) of the main text.

**S3.6. Weakly non-linear perturbation.** Eq. (S53) clearly highlights the relevant perturbation parameter in the problem as

$$\delta = \gamma(\epsilon - \epsilon^*) \ll 1 \quad [\text{S54}]$$

such that

$$\bar{W}'''' + 2\bar{W}'' + \bar{W} - \delta \frac{(\bar{x} - \bar{L}/2)^2}{2} \bar{W}'' = 0. \quad [\text{S55}]$$

We now solve Eq. (S55) perturbatively, by means of the following Ansatz

$$\bar{W}(\bar{x}) = A(\delta^{1/4}\bar{x})e^{i\omega\bar{x}} + \text{c.c.} \quad [\text{S56}]$$

where  $A$  is a slow-varying amplitude function that depends on the slow variable  $X = \delta^{1/4}\bar{x}$  and c.c. stands for complex conjugate. By the chain rule, we have

$$\bar{W}'(\bar{x}) = (i\omega A + \delta^{1/4}\partial_X A)e^{i\bar{x}} + \text{c.c.} \quad [\text{S57a}]$$

$$\bar{W}''(\bar{x}) = (-\omega^2 A + 2i\omega\delta^{1/4}\partial_X A + \sqrt{\delta}\partial_X^2 A)e^{i\bar{x}} + \text{c.c.} \quad [\text{S57b}]$$

$$\bar{W}'''(\bar{x}) = (\omega^4 A - 4i\omega^3\delta^{1/4}\partial_X A - 6\omega^2\sqrt{\delta}\partial_X^2 A + 4i\omega\delta^{3/4}\partial_X^3 A + \delta\partial_X^4 A)e^{i\bar{x}} + \text{c.c.} \quad [\text{S57c}]$$

where  $\partial_X = \partial/\partial X$ . We then insert Eq. (S57) into Eq. (S55), collect terms at various orders in  $\delta^{1/4}$  and obtain the following equations:

$$\mathcal{O}(\delta^0): \quad (\omega^4 - 2\omega^2 + 1)A = 0 \Rightarrow \omega = \pm 1 \quad [\text{S58}]$$

$$\mathcal{O}(\delta^{1/4}): \quad -4i\partial_X A + 4i\partial_X A = 0 \Rightarrow \text{OK} \quad [\text{S59}]$$

$$\mathcal{O}(\delta^{1/2}): \quad -6\partial_X^2 A + 2\partial_X^2 A + \frac{(X - X_e)^2}{2}A = 0, \quad [\text{S60}]$$

rewrite Eq. (S51) as:

$$\bar{W}'''' + 2\bar{W}'' + \bar{W} - \delta^{1/2} \frac{(X - X_e)^2}{2} \bar{W}'' - \delta^{3/4}(X - X_e)\bar{W}' = 0 \quad [\text{S52}]$$

Thus, the last term in Eq. (S52) enters our weakly non linear analysis only at order  $\delta^{3/4}$ , and consequently does not contribute to the order  $\delta^{1/2}$  amplitude equation Eq. (S61).

where  $X_e = \delta^{1/4} \bar{L}/2$ . From the  $\mathcal{O}(\delta^0)$  equation, we obtain  $\omega = 1$ , which implies that the oscillating part of the solution is  $e^{i\bar{x}}$ ; in terms of the original units, this means  $e^{ix/\lambda}$ , i.e. the wavelength of the oscillating field is  $\lambda$ . The order  $\delta^{1/4}$  equation is trivial. The order  $\delta^{1/2}$  equation corresponds to the amplitude equation (describing the long-scale behavior):

$$\partial_X^2 A = \frac{(X - X_e)^2}{8} A, \quad [\text{S61}]$$

which is Eq. (8) of the main text. This amplitude equation is a particular case of the Weber differential equation

$$y''(z) + \left( \nu + \frac{1}{2} - \frac{z^2}{4} \right) y(z) = 0 \quad [\text{S62}]$$

with  $\nu = -1/2$ , whose solution is expressed in terms of the parabolic cylinder function (sometimes called Weber function)

$$y(z) = D_\nu(z). \quad [\text{S63}]$$

Hence the envelope function is:

$$A(X) = C \cdot D_{-1/2} \left( \frac{X - X_e}{2^{1/4}} \right) \quad [\text{S64}]$$

Inserting the amplitude function back into Eq. (S56) and transforming back to the original variable  $x$ , we find the final solution for the vertical displacement:

$$W(x) = C \sqrt{\epsilon - \epsilon^*} \lambda \cos \left( \frac{x}{\lambda} \right) D_{-1/2} \left[ (\epsilon - \epsilon^*)^{1/4} \left( \frac{G}{B} \right)^{1/4} \left( x - \frac{L}{2} \right) \right]. \quad [\text{S65}]$$

The accuracy of the analytical approximation against numerics is shown in Figs. S9 and S10.

**S3.7. Energy scalings for localized solution.** We now discuss in detail the effect of geometric localization on the various contributions to elastic energy.

**S3.7.1. Shear energy.** The shear energy is zero for  $\epsilon < \epsilon^*$ ; for  $\epsilon > \epsilon^*$  it can be estimated using the outer solution for  $U(x)$ , Eq. (S47), yielding:

$$\begin{aligned} \mathcal{E}_G &= \frac{G}{2} \int_{-L/2}^{L/2} U(x)^2 dx \simeq G \int_0^{L/2} (\epsilon - \epsilon^*)^2 \left( x - \frac{L}{2} \right)^2 dx \\ &\simeq G (\epsilon - \epsilon^*)^2 \frac{L^3}{24}. \end{aligned} \quad [\text{S66}]$$

Thus, localization leads to a shear energy proportional to shear modulus  $G$  above  $\epsilon^*$ , Fig. S12(a).

**S3.7.2. Filament stretching energy.** Until the bifurcation point  $\epsilon^*$ , the stretching energy of the filament increases as

$$\mathcal{E}_S \simeq \frac{S}{2} \epsilon^2 L \quad [\text{S67}]$$

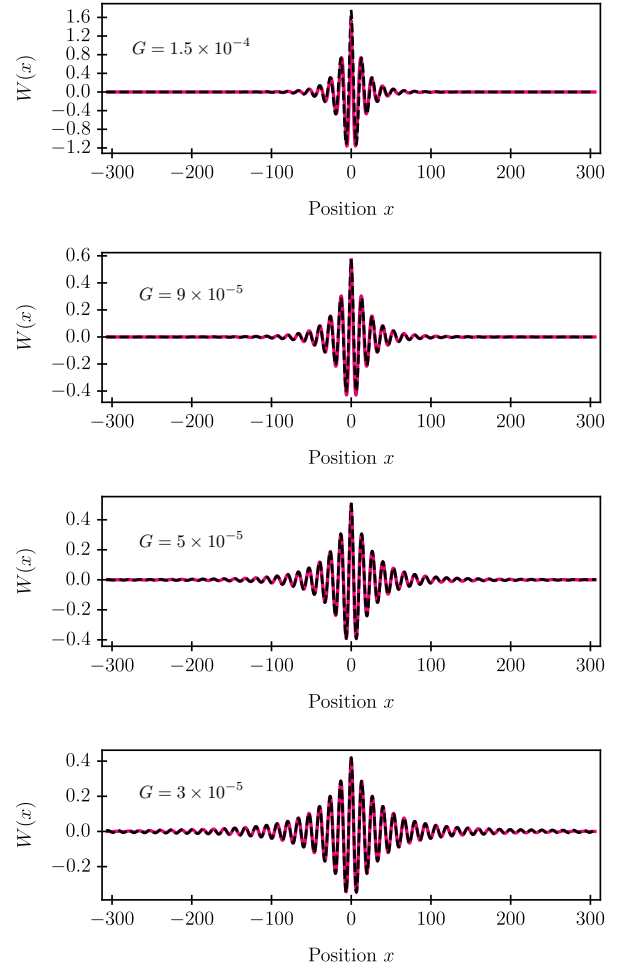


**Fig. S9.** Comparison between numerical solution (solid line) for horizontal displacement  $W$  and the perturbative solution Eq. (S65) (black dotted line) for different values of shear modulus (between  $G = 3 \times 10^{-5}$  and  $G = 1.5 \times 10^{-4}$ ). The parameters are:  $S = 10$ ,  $B = 0.2$ ,  $K = 0.01$ ,  $\epsilon = 9.5 \times 10^{-3}$ ,  $L = 23 \times \lambda$ .

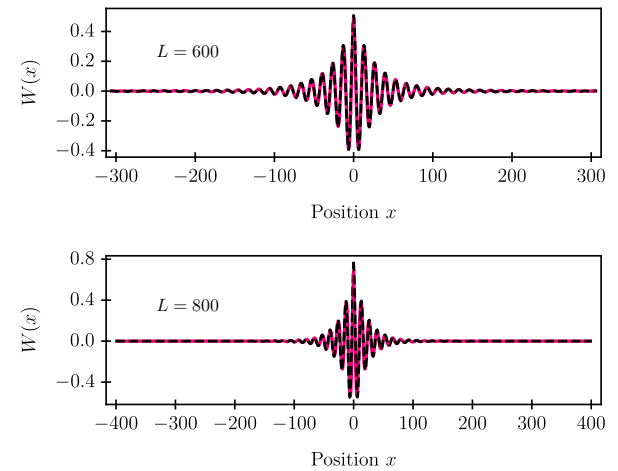


**Fig. S10.** Comparison between numerical solution (solid line) for horizontal displacement  $W$  and the perturbative solution Eq. (S65) (black dotted line) for  $L = 23 \times \lambda$  (top) and  $L = 30 \times \lambda$  (bottom). The parameters are:  $G = 5 \times 10^{-5}$ ,  $S = 10$ ,  $B = 0.2$ ,  $K = 0.01$ ,  $\epsilon = 9.5 \times 10^{-3}$ .

To estimate the stretching energy in the localized state beyond  $\epsilon^*$ , we use Eq. (S46) and find

$$\begin{aligned} & \frac{S}{2} \left[ \epsilon^* + (\epsilon - \epsilon^*) - U'(x) - \frac{W'(x)^2}{2} \right]^2 \\ & \simeq \frac{S}{2} \left[ \epsilon^* - (\epsilon - \epsilon^*) \frac{\alpha}{\lambda^2} \frac{(x - L/2)^2}{2} \right]^2 \\ & \simeq \frac{S}{2} (\epsilon^*)^2 - S\epsilon^* \frac{\alpha}{\lambda^2} \frac{(x - L/2)^2}{2} (\epsilon - \epsilon^*) + \dots \\ & \simeq \frac{S}{2} (\epsilon^*)^2 - \frac{S}{2} (\epsilon^*)^2 \frac{G}{\sqrt{KB}} \frac{(x - L/2)^2}{2} (\epsilon - \epsilon^*) + \dots \quad [\text{S68}] \end{aligned}$$

where we used  $\alpha = \gamma/\sigma$  and  $\epsilon^* = 2/\sigma$ . Hence, in the localized state, stretching energy above the bifurcation point  $\epsilon^*$  is reduced by an amount proportional to  $G$  compared to the uniform wrinkled solution. The stretching energy for  $\epsilon > \epsilon^*$  is thus estimated as

$$\mathcal{E}_S \simeq \frac{S}{2} (\epsilon^*)^2 L \left[ 1 - \frac{G}{\sqrt{KB}} \frac{L^2}{24} (\epsilon - \epsilon^*) \right]. \quad [\text{S69}]$$

Localization reduces the filament stretching energy by an amount proportional to  $G$ , Fig. S12(b).

**S3.7.3. Filament bending and spring energies.** Filament bending and spring energies are zero for  $\epsilon < \epsilon^*$ ; for  $\epsilon > \epsilon^*$ , they can be estimated as

$$\mathcal{E}_B = \frac{B}{2} \int_{-L/2}^{L/2} W''(x)^2 dx \simeq \frac{B}{2} \left( \frac{A}{\lambda^2} \right)^2 \min\{w, L\}, \quad [\text{S70}]$$

respectively,

$$\mathcal{E}_K = \frac{K}{2} \int_{-L/2}^{L/2} W(x)^2 dx \simeq \frac{K}{2} A^2 \min\{w, L\} \quad [\text{S71}]$$

where  $A$  is the amplitude of the localized state,  $w$  its width. Since  $\lambda = (B/K)^{1/4}$ , we find that  $\mathcal{E}_B = \mathcal{E}_K$ , hence we focus only on spring energy. Using Eq. (S65), we find

$$\begin{aligned} \mathcal{E}_K & \simeq \frac{K}{2} A^2 w \simeq \frac{K}{2} (\epsilon - \epsilon^*) \left( \frac{G}{K} \right)^{1/2} \lambda L \cdot (\epsilon - \epsilon^*)^{-1/4} \left( \frac{G}{B} \right)^{-1/4} \\ & \simeq \frac{\sqrt{BK}}{2} (\epsilon - \epsilon^*)^{3/4} \left( \frac{G}{K} \right)^{1/4} L \quad [\text{S72}] \end{aligned}$$

Localization modifies the dependence of bending and spring energy on  $\epsilon - \epsilon^*$ , Fig. S12(c). To understand the conditions under which the localized solution has lower energy than the uniform one, we compare the expression Eq. (S72) with Eq. (S34); due to the different dependencies on  $\epsilon - \epsilon^*$ , there is a critical value for the strain  $\epsilon$  above which localized deformations become energetically favorable (Fig. S12(c)):

$$\begin{aligned} \frac{\sqrt{BK}}{2} (\epsilon - \epsilon^*) L & \simeq \frac{\sqrt{BK}}{2} (\epsilon - \epsilon^*)^{3/4} \left( \frac{G}{K} \right)^{1/4} L \\ \Rightarrow (\epsilon - \epsilon^*)_{\text{crit}} & \simeq \frac{G}{K} \quad [\text{S73}] \end{aligned}$$

Thus, upon increasing  $\epsilon$ , the localized solution becomes energetically more favorable than the uniformly wrinkled solution. The critical value of  $\epsilon$  above which the localized solution has lower energy depends on the values of  $G$  and  $K$ ; increasing  $G$  or decreasing  $K$  increases the value of  $\epsilon$  at which the localized solution will branch off. This conclusion is confirmed by numerical simulations (Fig. S13).

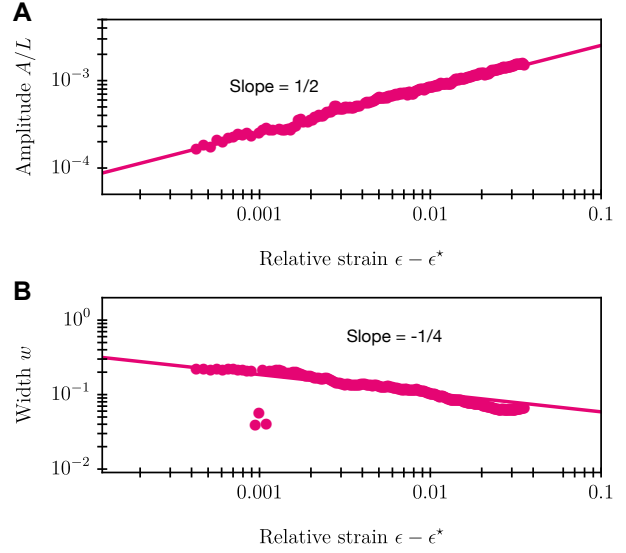


**Fig. S11.** Scaling behavior of amplitude (a) and width (b) with excess strain  $\epsilon - \epsilon^*$  from simulations of discrete rod model is compared to analytical predictions of Eq. (9) and (10) of the main text. These predict: the amplitude scales as  $(\epsilon - \epsilon^*)^{1/2}$ , while the width scales as  $(\epsilon - \epsilon^*)^{-1/4}$ .

## References

1. J. Burke and E. Knobloch. *Snakes and ladders: localized states in the Swift-Hohenberg equation*. Phys. Lett. A 360(6):681-688 (2007).
2. E. Winkler. *Die Lehre von der Elastizität und Festigkeit*. (Dominicus, Prague, 1867).
3. M.C. Cross, P.C. Hohenberg (1993) *Pattern formation outside of equilibrium*. Rev. Mod. Phys. 65:851.

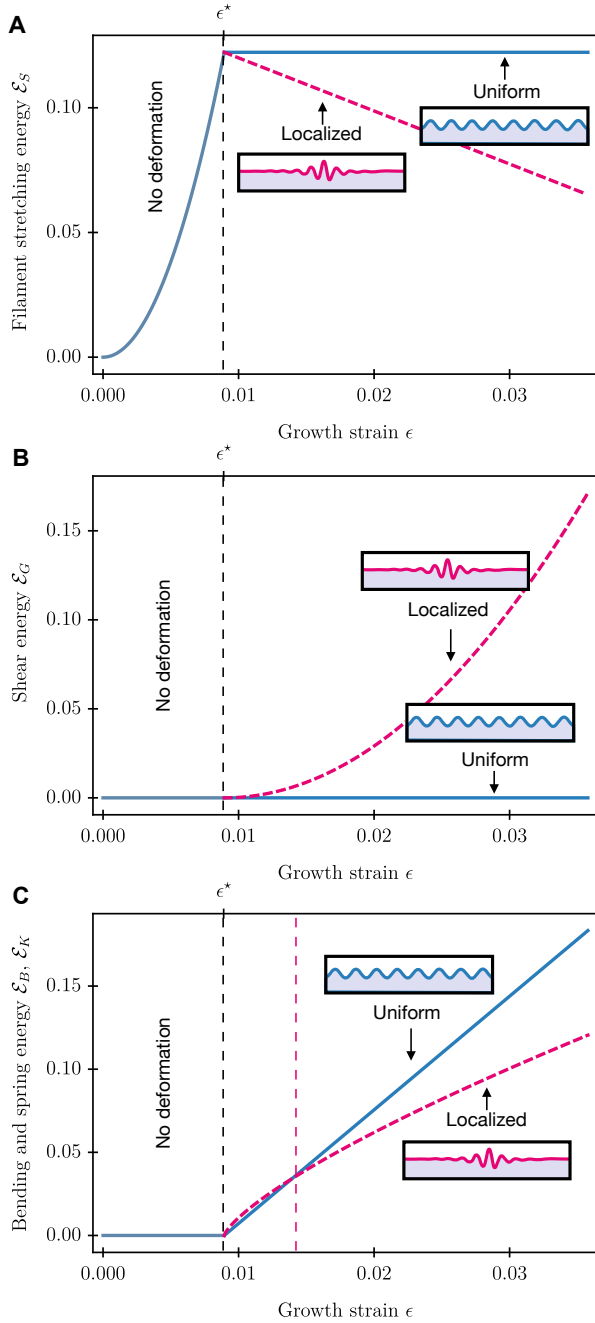


**Fig. S12.** (a) Shear energy, (b) filament stretching energy, (c) filament bending and spring energy for uniform (solid line) and localized (dashed line) deformations as a function of growth strain  $\epsilon$  (Eq. (S66), Eq. (S69), and Eq. (S72)). The parameters are:  $G = 5 \times 10^{-5}$ ,  $S = 10$ ,  $B = 0.2$ ,  $K = 0.01$ ,  $\epsilon = 9.5 \times 10^{-3}$ ,  $L = 23 \times \lambda$ .

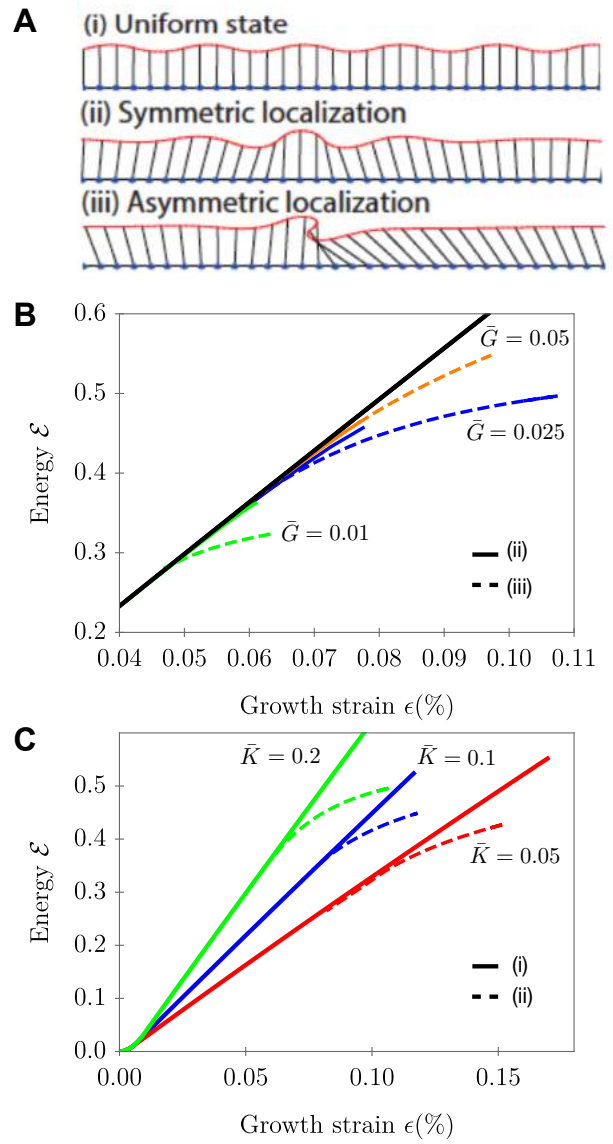


**Fig. S13.** (a) Three solution branches: (i) uniform buckling, (ii) symmetric localized structure and (iii) asymmetric localized structure. Total energy of the system as function of the growth strain  $\epsilon$  for (b) various shear moduli  $\bar{G}$  and (c) various substate stiffness  $\bar{K}$ . The black solid line is the uniform solution (i), the colored lines are the symmetric solutions (ii) and the dashed lines are the antisymmetric (iii).